

REPORT DOCUMENTATION PAGE

Form Approved
OMB NO. 0704-0188

Public Reporting burden for this collection of information is estimated to average 1 hour per response, including the time for reviewing instructions, searching existing data sources, gathering and maintaining the data needed, and completing and reviewing the collection of information. Send comment regarding this burden estimates or any other aspect of this collection of information, including suggestions for reducing this burden, to Washington Headquarters Services, Directorate for Information Operations and Reports, 1215 Jefferson Davis Highway, Suite 1204, Arlington, VA 22202-4302, and to the Office of Management and Budget, Paperwork Reduction Project (0704-0188), Washington, DC 20503.

1. AGENCY USE ONLY (Leave Blank)	2. REPORT DATE	October 31, 2003	3. REPORT TYPE AND DATES COVERED Final Report July 2000 to April 2003
4. TITLE AND SUBTITLE Semiconductor Nanostructures on High Index Surfaces		5. FUNDING NUMBERS DAAD19-00-1-0442	
6. AUTHOR(S) Elias Towe			
7. PERFORMING ORGANIZATION NAME(S) AND ADDRESS(ES) Box 400258 University of Virginia Charlottesville, Virginia 22904-4258		8. PERFORMING ORGANIZATION REPORT NUMBER 41625.1-EL	
9. SPONSORING / MONITORING AGENCY NAME(S) AND ADDRESS(ES) U. S. Army Research Office P.O. Box 12211 Research Triangle Park, NC 27709-2211		10. SPONSORING / MONITORING AGENCY REPORT NUMBER 41625.1-EL	
11. SUPPLEMENTARY NOTES The views, opinions and/or findings contained in this report are those of the author(s) and should not be construed as an official Department of the Army position, policy or decision, unless so designated by other documentation.			
12 a. DISTRIBUTION / AVAILABILITY STATEMENT Approved for public release; distribution unlimited.		12 b. DISTRIBUTION CODE	
13. ABSTRACT (Maximum 200 words) This report summarizes work on semiconductor quantum dot nanostructures that was carried out at the University of Virginia from July 2000 to April 2003. The key findings of the work are that: the emission and absorption properties of these nanostructures are intimately linked to the control of their size and ordering. The size of the quantum dot nanostructures was found to be more dominant in affecting the optical properties of the structures. It was determined that the dots could be ordered in the vertical direction. This ordering, however, led to a reduction in the in-plane areal density. Some minimal in-plane ordering could be achieved when the structures are grown on high index surfaces. The best surface for dot uniformity (without lateral ordering) was the (001) surface mis-oriented by 1 to 2 degrees. In this configuration, the surface can technically be represented as a high index surface. Semi-analytical calculations have been carried out to determined the energy structure of the dot nanostrucutres. These calculations were used in some of the experimental studies reported in the attached papers. These studies were carried out on quantum dot inter-band as well as intra-band laser and photodetector structures.			
14. SUBJECT TERMS Nanostructures, Quantum Dots, Semiconductors, Inter-sublevel, Intraband, interband, Lasers Photodetectors,		15. NUMBER OF PAGES 7	
		16. PRICE CODE	
17. SECURITY CLASSIFICATION OR REPORT UNCLASSIFIED	18. SECURITY CLASSIFICATION ON THIS PAGE UNCLASSIFIED	19. SECURITY CLASSIFICATION OF ABSTRACT UNCLASSIFIED	20. LIMITATION OF ABSTRACT UL

NSN 7540-01-280-5500

Standard Form 298 (Rev.2-89)
Prescribed by ANSI Std. Z39-18
298-102

20031204 080

List of Appendices

Papers Published in Peer-reviewed Journals (4 out of 10 attached)

1. V. G. Stoleru, D. Pal, and E. Towe, "Self assembled InGaAs/GaAs quantum dot nanostructures: strain distribution and electronic structure," *Physica E* 15 (3), 131-152, (2002).
2. D. Pal, D. Firsov, and E. Towe, "Interband emission and normal-incidence intraband absorption in (In,Ga)As quantum-dot nanostructures," *Physica E* , 15 (1), 6-12 (2002).
3. L. Chen, V.G. Stoleru, D. Pan, and E. Towe, "Enhanced 1.3-mm-emission from InAs quantum dots embedded in symmetric (In,Ga)As quantum-well structures," *J. Crystal Growth*, 242, 263-269 (2002).
4. D. Pal, G. Stoleru, D. Firsov and E. Towe, "Quantum dot-size variation and its impact on emission and absorption characteristics: an experimental and theoretical modeling investigation," *Jpn. J. Appl. Phys.*, 41 (2A), 482-489 (2002).

Introduction

It is now well established that self-assembled (In,Ga)As quantum dots grown on GaAs substrates can absorb infrared radiation in the spectral region from 5.0 to 14 μm . The absorption is due to inter-sublevel transitions in the conduction band of the (In,Ga)As structures. When used in the active regions of light sources, properly designed quantum dots can be caused to emit light from about 890 through 1350 nm. The access to these extended spectral regions that the quantum dots provide, especially when the technologically advanced and robust GaAs-based materials system is used, has generated a lot of excitement and interest in the area of quantum dot research. A number of problems still remain after the preliminary demonstration of devices based on these nanostructures.

Statement of the Problem

The potential for the use of the quantum dots in mid- infrared detectors and near-infrared lasers remains to be realized. Our initial results, and those from other researchers in the field, have revealed a number of problems associated with the use of the dots in photodetectors and lasers. The key problems are connected with (i) uniformity and control of the dot size, (ii) optimization of device structures and the spatial location of dopant impurity atoms, and (iii) lack of in-plane lateral ordering of the dots. These problems manifest themselves in a number of ways in real devices. In lasers, the lack of size uniformity leads to irreproducible wavelengths of emission, and in photodetection, it leads to broad and variable absorption lines. The lack of lateral order leads to unpredictable threshold currents in lasers. In detectors, dot non-uniformity and improper doping lead to detector noise and hence low detectivity.

Summary of Key Findings

During the research period covered in this report, we studied the structural characteristics of the quantum dots, both theoretically and experimentally. The theoretical analysis was undertaken to understand the important physical variables (size, mole fraction, strain) and how they control the electronic structure and hence the emission or absorption wavelengths do the dots. The experimental study was undertaken

to validate the theory, and with guidance from the analytical understanding, find out new ways to better engineer and build the structures for use in device applications. Experimentally, it was found that ordering of the quantum dot nanostructures could be induced in the vertical direction on both high index surfaces as was as on the conventional (001) surface. Lateral ordering was much more difficult on either substrate surface.

The first key result is from our theoretical work and it was the demonstration that a semi-analytical method could be used to provide the energy structure of the dots. The method we developed is described in detail in Reference [1]. A copy of the published paper is attached to this report. The appeal of the method we developed is that solutions to the band structure of the dots can be rapidly obtained without recourse to the traditional methods that require intensive computational effort [2,3], including in some cases, the use of a super computer. The solutions obtained using our method are found to be in compete agreement with those obtained using the more computationally intensive methods. Furthermore, our theoretical results agree with our experimental measurements. The method we have developed therefore has become a useful tool in our experimental investigations of devices fabricated from (In,Ga)As quantum dots. We have confirmed both experimentally and theoretically that most dots grown in our laboratory are pyramidal in shape, but with "truncated" tops.

A second key result was from our experimental work. We demonstrate that by embedding quantum dots in symmetrically graded quantum wells, the near-infrared emission of the dots can be enhanced by as much as an order of magnitude. We further showed that the emission wavelengths of such dots can be extended to the 1300 nm range, which is a of technological importance. Silica-based fibers for communication exhibit an absorption and a dispersion minimum at 1300 nm. The results have been reported n the literature [4] and a copy of the published paper is attached to this report.

A third key finding from our work is that when the (In,Ga)As quantum dots are used to fabricated infrared inter-sublevel detectors, the noise in these devices is primarily due to generation -recombination noise between 78 K – 100 K. This can be reduced by improving the quality of the structures. In particular, one can obtain results by improving the electron mobility and lowering the defects in the device structures.

The fourth finding is that the quantum size variation leads to broad and random absorption lines. These results have been reported in the technical literature [5] and a copy of the published paper is attached to this report.

Peer-Reviewed Technical Papers Supported Under Contract DAAD19-00-1-0442

1. D. Pal, G. Stoleru, D. Firsov and E. Towe, "Quantum dot-size variation and its impact on emission and absorption characteristics: an experimental and theoretical modeling investigation," *Jpn. J. Appl. Phys.*, 141 (2A), 482-489 (2002).
2. D. Pal, D. Firsov, and E. Towe, "Interband emission and normal-incidence intraband absorption in (In,Ga)As quantum-dot nanostructures," *Physica E*, 15 (1), 6-12 (2002).
3. V. G. Stoleru, D. Pal, and E. Towe, "Self assembled InGaAs/GaAs quantum dot nanostructures: strain distribution and electronic structure," *Physica E* 15 (3), 131-152, (2002).
4. L. Chen, V.G. Stoleru, D. Pan, and E. Towe, "Enhanced 1.3-mm-emission from InAs quantum dots embedded in symmetric (In,Ga)As quantum-well structures," *J. Crystal Growth*, 242, 263-269 (2002).
5. L. Chen, V. G. Stoleru, and E Towe, "Improved luminescence from quantum-dot nanostructures embedded in structurally engineered (In,Ga)As confining layers," *IEEE J. Selected Topics in Quantum Electronics*, 8, 1045-1050 (2002).
6. E. Towe, D. Pal, L. E. Vorobjev, A. V. Gluhovskoy, S. N. Danilov, V. I. Zerova, V. Yu. Panarin, D. A. Firsov, V. A. Shalygin, G. G. Zegrya, A. Weber, M. Grudmann, "Injection lasers based on intraband carrier transitions," *Materials Science Forum*, 384-385, 209-212, (2002).

7. L. E. Vorobjev, S. N. Danilov, A. V. Gluhovskoy, L. L. Zerova, E. A. Zibik, V. Yu. Panevin, D. A. Firsov, V. A. Shalygin, A. D. Andreev, B. V. Volovik, A. E. Zhukov, N. N. Ledentsov, D. A. Livshits, V. M. Ustinov, Yu. M. Shernyakov, A. F. Tsasulnikov, A. Weber, M. Grundmann, S. R. Schmidt, A. Seilmeier, E. Towe, and D. Pal, "Optical phenomenon connected with intraband carrier transitions in quantum dots and quantum wells," *Nanotechnology*, 12 462-465, (2001).
8. A. Kastalsky, L. E. Vorobjev, D. A. Firsov, V. L. Zerova, E. Towe, J. Cockburn, and M. Skolnick, "A dual-color semiconductor injection laser based on intra- and inter-band carrier transitions in semiconductor quantum wells or quantum dots," *IEEE J. Quantum Electron.*, 37(10) 1356-1362 (2001).
9. D. Pal, D. Pan, E. Towe, and S. J. Chen, "Characterization of (In,Ga,Al)As/GaAs quantum-dot superlattice structures by high-resolution x-ray diffraction," *J. Cryst. Growth*, 233, 34-39 (2001).
10. D. Pal, E. Towe, and S. J. Chen, "Structural characterization of InAs/GaAs quantum-dot nanostructures," *Appl. Phys. Lett.*, 78(26) 4133-4135 (2001).

Personnel Supported Under Contract DAAD19-00-1-0442

1. Liang Chen
2. Debdas Pal
3. Dong Pan
4. Gabriella Stoleru

* Earned the PhD degree under the support of contract DAAD19-00-0442

References

1. V. G. Stoleru, D. Pal, and E. Towe, *Physica E* 15 (3), 131-152, (2002).
2. M. Grudmann, O. Steir, D. Bimberg, *Phys. Rev. B* 54 11969 (1995).
3. M. A. Cusack, P. R. Briddon, M. Jaros, *Phys. Rev. B* 54 R2300 (1996).
4. L. Chen, V.G. Stoleru, D. Pan, and E. Towe, *J. Crystal Growth*, 242, 263-269 (2002).
5. D. Pal, G. Stoleru, D. Firsov and E. Towe, *Jpn. J. Appl. Phys.*, 41 (2A), 482-489 (2002).

Self-assembled (In,Ga)As/GaAs quantum-dot nanostructures: strain distribution and electronic structure

Valeria-Gabriela Stoleru^{a,*}, Debdas Pal^b, Elias Towe^b

^a*Laboratory for Optics and Quantum Electronics, Department of Electrical and Computer Engineering, University of Virginia, Charlottesville, VA 22904-4743, USA*

^b*Laboratory for Photonics, Department of Electrical and Computer Engineering, Carnegie Mellon University, Pittsburgh, PA 15213, USA*

Received 30 October 2001; accepted 13 March 2002

Abstract

This paper presents a simple analytical method for calculating the strain distribution in and around self-assembled (In,Ga)As/GaAs quantum-dot nanostructures. The dots are assumed to be buried in an infinite medium so that the effects of free surfaces can be neglected. This assumption is based on the relative size of the dot, compared to that of the overlayer. The model—based on classical continuum elasticity—is capable of handling dots of arbitrary shapes; here, however, only dots with pyramidal and truncated-pyramidal shapes are considered. The approximate shape of the dots is extracted from high-resolution transmission electron microscope observations. The electronic energy levels in the dots are calculated by solving the three-dimensional effective mass Schrödinger equation. The carrier confinement potential in this equation is modified by the strain distribution. Because the dots are in a strong confinement regime, the effects of Coulomb interactions are neglected. The calculated confined eigen-energies agree with our experimental photoluminescence data. The calculations also support previous results reported by others. © 2002 Elsevier Science B.V. All rights reserved.

PACS: 83.85.St; 73.21.La; 68.66.Hb; 68.37.Lp; 73.43.Cd

Keywords: Quantum dots; Strain; Eight-band model; Electronic spectra; Nanostructures

1. Introduction

Progress in nanotechnology has resulted in the synthesis of nanometer-scale self-assembled quantum dots for potential applications in electronics and optoelectronics. Several devices that include quantum dots in their active regions have been proposed in the past few years; some of them, such as lasers, infrared detectors, and memory elements have been

demonstrated. Since millions of dots are generally required to yield macroscopic effects, a narrow-size distribution is important for optimum device performance. The synthesis of uniform-sized dots is still a research problem and much remains to be learned in understanding the growth processes that lead to pristine and uniform-sized quantum dots. The most studied quantum-dot system today is based on the spontaneous formation of (In,Ga)As islands on a GaAs substrate during heteroepitaxy. This process is a consequence of the strain which results from the in-plane lattice-mismatch between the (In,Ga)As and the GaAs. The specific shape of the dots is usually

* Corresponding author.

E-mail addresses: gstoleru@virginia.edu (V.-G. Stoleru), towe@cmu.edu (E. Towe).

a function of the growth parameters and the general environment of the dots. Some researchers have observed dots with hemispherical shapes; others have observed dot-shapes that are multifaceted domes; and yet several other groups have reported dots with pyramidal shapes [1]. It is generally difficult to determine the shape of the dots *in situ* during growth; the lateral extent and height of the dots, however, can often be determined approximately for surface quantum dots from atomic force microscope studies. Better estimates of buried dot-sizes can usually be obtained from transmission electron microscope studies; these studies can generally provide valuable information about the shape of the dots [2]. Central to understanding many properties of the dot is a need to determine the elastic strain distribution in and around the dots. The strain distribution profoundly affects the electronic structure, and hence the optical properties of the dots by modifying the energies and wave functions for confined carriers. The principal aim of this paper is to quantitatively determine the stress fields and hence the strain distribution in and around a dot. This information is then used to calculate the electronic structure of the dots.

Strain drives the Stranski–Krastanow growth process that leads to the formation of dots; residual strain, in general, can have interesting effects on the electronic and optical properties of semiconductor structures. The effects of strain on semiconductors have therefore motivated a significant interest in calculating its magnitudes in a broad range of devices [3]. The hydrostatic (ϵ_h) component of strain, for example, usually shifts the conduction and valence band-edges of semiconductors; biaxial (ϵ_b) strain, on the other hand, modifies the valence bands by splitting the degeneracy of the light- and heavy-hole bands. These effects have a profound impact on the electronic and optical properties of the structures out of which devices might be fabricated.

The two general classes of techniques used in the calculation of strain include the finite difference [4,5] and atomistic calculation methods [6]. Both of these methods require considerable computational resources. In the atomistic approach, there is an implicit reliance on the validity of the valence force field model with a Keating interatomic potential. This method, however, has recently been shown to be questionable for small islands whose base dimen-

sions are smaller than 10 nm [7]; for these islands, the Stillinger–Weber potential has been suggested as an alternative potential. The finite element and finite difference methods have been used by several groups [4,8–11]. One advantage of the finite element and finite difference methods is that they can be used to treat problems with complex geometries. This advantage, however, is offset by the demand on computational resources. Another variant of these methods is the boundary element approach; this, however, can be mathematically complex [12]. A simple and elegant method for calculating strain fields around a single, isotropic, cubic dot has been presented by Downes et al. [13]. This method is based on a simplification of Eshelby's classic inclusion theory [14]. The method first identifies a set of vectors such that the divergence of each gives the Green's function for the stress components σ_{ij} . By invoking Gauss' theorem, the stress field is determined by performing an integral over the surface of the dot.

In this paper, we extend the method to more complex and practical geometries. We particularly focus on regular pyramids and those with truncated tops. In the model, we make the basic assumption that the elastic properties of the materials are isotropic [15]. This assumption does not seriously affect any qualitative conclusions drawn from the calculations. In any event, it has been shown in a recent paper [16] that as long as the symmetry of the shape of the structure is less than or equal to the cubic symmetry of the crystal, both anisotropic and isotropic models give similar results. We caution however that even though this is true for quantum-dot nanostructures, it is not so for quantum-well heterostructures.

Our calculations here are for the (In,Ga)As/GaAs materials system. The model, however, is general enough that it can be used for similar other materials systems. For the InAs/GaAs system, the initial strain or lattice-mismatch is defined as $\epsilon_0 = (a_{\text{GaAs}} - a_{\text{InAs}})/a_{\text{InAs}} = -0.067$. This is the fractional change of the difference between the in-plane lattice constant of the GaAs substrate and the InAs epilayer with respect to the InAs lattice constant; when Ga is included in the composition of the epilayer, the mismatch (strain) becomes $\epsilon_0 = (a_{\text{GaAs}} - a_{\text{In}_x\text{Ga}_{1-x}\text{As}})/a_{\text{In}_x\text{Ga}_{1-x}\text{As}}$. The Poisson ratios for the binary materials are taken to be 0.316 for the GaAs and 0.354 for the InAs. As is usual in continuum elasticity, we assume that the

materials are continuous, linear, isotropic, and obey Hooke's law. The use of continuum elasticity methods has been experimentally verified to be valid for layers as thin as three atomic monolayers [17]; furthermore, it is estimated theoretically that the method remains valid for layers whose thicknesses are on the order of five atoms [18]. We want to point out that the sensitivity of some physical properties to strain could make anisotropic effects important; the isotropic approximation should therefore be treated with caution, particularly for layers oriented in certain crystallographic directions. For most cases, however, the anisotropy only modifies the strain distributions slightly [16,19].

Classical elasticity and atomistic methods have been shown to give similar results for small strains [20]. Differences become apparent for strains larger than 5%, particularly in the case of semiconductor quantum dots. Even though atomistic elasticity is expected to continue to give reliable results for large strains, the number of atoms involved in the computations makes the method unwieldy for rapid, order-of-magnitude calculations. The advantage of the approach based on Eshelby's inclusion theory is that it is simple and allows one to find approximate analytical expressions for the strain tensor components. As we will show later, for quantum dots with lateral dimensions in the range of 10–20 nm, the strain profiles calculated within the modified Eshelby framework are in good agreement with those obtained by the methods of atomistic elasticity.

This paper is organized as follows: in Section 2 we give a detailed description of the basic model for calculating the strain tensor for pyramidal and truncated pyramidal quantum dots. The strain fields are presented and discussed in Section 3. The method discussed here is a suitable precursor for the calculation of electronic structure based on the envelope function method within the plane-wave expansion technique. One can determine, for example, the strain-dependent matrix element linking any pair of plane waves. We present and discuss the strain-dependent confining potentials for electrons and holes, as well as the electronic energy levels in Section 4. A summary of our results is given in Section 5.

In our calculations, we consider a single isolated dot to facilitate comparison with published results. The dot is assumed to be buried deep within a matrix material.

Figs. 1(a) and (b) show the schematic cross-sections of the pyramidal and truncated pyramidal quantum-dot structures under consideration. They are assumed to be on top of a semi-infinite (0 0 1) GaAs substrate on which is grown a thin InAs wetting layer first.

2. Model description

Most theoretical calculations of the properties of InAs dots assume a square-based pyramidal shape [4,6,21]. Here, for purposes of comparison with previously published work, we also consider this geometry. However, we extend our calculations to include the truncated pyramidal case. When a capping layer—for example GaAs—is grown on top of a layer of dots, the morphology of the overlayer is affected by the interaction of the inhomogeneous strain around the dots and in the wetting layer. This affects the apex of the dots. There is then a thermodynamically favored tendency for the adatoms to migrate to the side of the dots [22], resulting in a reduction of the dot height and formation of a flat (0 0 1) top surface.

Following Downes et al. [13], the Lamé potential u during relaxation can be described by a scalar potential

$$u = \frac{1}{2G} \nabla \Phi, \quad (1)$$

where G is the shear modulus, defined as $2G = E/(1 + \nu)$ in Ref. [23]. The displacement potential obeys the Poisson equation

$$\nabla^2 \Phi(r) = \frac{1 + \nu}{1 - \nu} \varepsilon_0(r) 2G. \quad (2)$$

From Eq. (2), a solution can be reached by integration, using Green's function, thus

$$\frac{1}{2G} \Phi(r) = -\frac{(1 + \nu)}{(1 - \nu)} \iiint_V \frac{\varepsilon_0(r_0)}{4\pi|r - r_0|} d^3 r_0. \quad (3)$$

In the equation above, the function $1/|r - r_0|$ can be written as

$$-\frac{1}{2} \vec{\nabla} \cdot \frac{(r - r_0)}{|r - r_0|}.$$

The point r_0 is within the volume of the dot. The volume integral in Eq. (3) can be converted to a surface integral by applying the divergence theorem to it, with

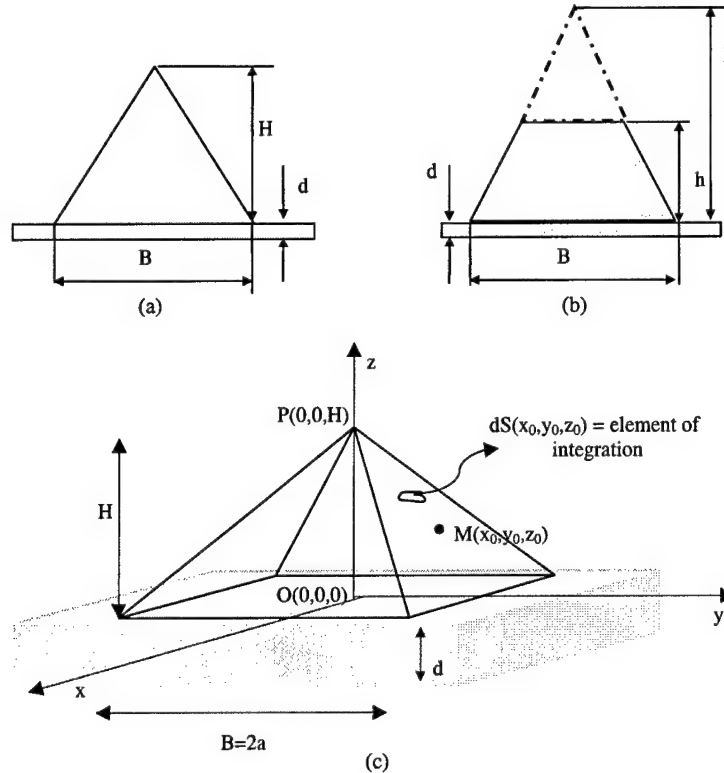


Fig. 1. Schematic models for the pyramidal (a) and truncated pyramidal (b) quantum-dot structures; B = base width, H = pyramid height, t = truncation factor, h = truncated pyramid height, d = thickness of wetting layer; (c) Three-dimensional model of a quantum dot in the Cartesian coordinate system.

the point r_0 now being on the surface of the dot, as shown in Fig. 1(c). Thus

$$\begin{aligned} \frac{1}{2G} \Phi(r) &= \frac{1}{8\pi} \frac{(1+\nu)}{(1-\nu)} \\ &\times \iiint_V \varepsilon_0(r_0) \vec{\nabla} \cdot \frac{(r-r_0)}{|r-r_0|} d^3 r_0 \\ &= \frac{1}{8\pi} \frac{(1+\nu)}{(1-\nu)} \\ &\times \iint_S \varepsilon_0(r_0) \frac{(r-r_0)}{|r-r_0|} dS(r_0). \end{aligned} \quad (4)$$

The initial lattice-mismatch, ε_0 , can be considered constant within the volume of the dot. With the appropriate substitutions, Eq. (1) becomes

$$u = \frac{1}{2G} \nabla \Phi = \frac{\varepsilon_0}{4\pi} \frac{(1+\nu)}{(1-\nu)} \iint_S \frac{1}{|r-r_0|} dS(r_0). \quad (5)$$

The stress components can therefore be written as

$$\begin{aligned} \sigma_{ij}(r) &= -\frac{\varepsilon_0 E}{8\pi(1-\nu)} \\ &\times \iint_S \frac{(i-i_0)\hat{i} + (j-j_0)\hat{j}}{|r-r_0|^3} dS(r_0) \\ &+ \delta_{ij} \frac{E\varepsilon_0}{1-\nu} \iint_S \delta(r-r_0) dV(r_0), \end{aligned} \quad (6)$$

where \hat{i} and \hat{j} are unit vectors in the i th and j th directions, respectively, for $i = x, y, z$, $j = x, y, z$ and $r^2 = x^2 + y^2 + z^2$. The parameter ε_0 is the isotropic misfit strain, E is the Young's modulus, ν is Poisson's ratio, and δ_{ij} is the Kronecker delta function. The last part of Eq. (6) comes from evaluating the limit of the surface integral, as a field point r approaches the boundary point r_0 on the surface of the dot. The misfit strain is taken as negative for a material under compression.

The volume of a square-based, truncated pyramid is defined by

$$\begin{aligned} -B \frac{(H-z)}{2H} &\leq x \leq B \frac{(H-z)}{2H}, \\ -B \frac{(H-z)}{2H} &\leq y \leq B \frac{(H-z)}{2H}, \\ 0 &\leq z \leq Ht, \end{aligned} \quad (7)$$

where H is the height of the pyramid in the absence of truncation, B is the base of the pyramid, and $0 \leq t \leq 1$, where t represents the truncation factor. The z -axis is the $[001]$ growth direction, and the origin of the coordinates is at the center of the square base of the pyramid (the $z = 0$ plane).

After converting to Cartesian coordinates, the integrations indicated in Eq. (6) can be easily carried out. The in-plane stress components have cumbersome mathematical expressions; however, for some particular directions, they can be simplified. For example, for a square-based pyramidal dot, with a contrast ratio (defined as the ratio of the height to the base) of 1:2, where $B = 2a$ and $H = a$, one obtains the following expressions as functions of z :

$$\begin{aligned} \sigma'_{xx} &= \sigma'_{yy} \\ &= 2 \left[-\tan^{-1} \left(\frac{z-a}{|z-a|} \right) \right. \\ &\quad \left. + \tan^{-1} \left(\frac{z}{\sqrt{2a^2+z^2}} \right) \right] \\ &\quad + \frac{1}{2} \left[\ln \left| \frac{\sqrt{2a^2+z^2}-a}{\sqrt{2a^2+z^2}+a} \right| \right. \\ &\quad \left. - \ln \left| \frac{\sqrt{2a^2+z^2}+a}{\sqrt{2a^2+z^2}-a} \right| \right] \\ &\quad + \frac{2}{\sqrt{3}} \left[\ln \left(\frac{-(z-a)}{\sqrt{3}} + |z-a| \right) \right. \\ &\quad \left. - \ln \left(\frac{-2a-z}{\sqrt{3}} + \sqrt{2a^2+z^2} \right) \right], \end{aligned} \quad (8)$$

and

$$\begin{aligned} \sigma'_{zz} &= 4\pi - 4 \left[-\tan^{-1} \left(\frac{z-a}{|z-a|} \right) \right. \\ &\quad \left. + \tan^{-1} \left(\frac{z}{\sqrt{2a^2+z^2}} \right) \right] \\ &\quad + \left[\ln \left| \frac{\sqrt{2a^2+z^2}-a}{\sqrt{2a^2+z^2}+a} \right| - \ln \left| \frac{\sqrt{2a^2+z^2}+a}{\sqrt{2a^2+z^2}-a} \right| \right] \\ &\quad + \frac{4}{\sqrt{3}} \left[\ln \left(\frac{-(z-a)}{\sqrt{3}} + |z-a| \right) \right. \\ &\quad \left. - \ln \left(\frac{-2a-z}{\sqrt{3}} + \sqrt{2a^2+z^2} \right) \right]. \end{aligned} \quad (9)$$

Note that $\sigma_{ij} = E\varepsilon_0/(4\pi(1-\nu))\sigma'_{ij}$, where ε_0 , ν , and E are as defined before. The more general analytical expressions for calculating stress distributions in structures with arbitrary degrees of truncation are given in the Appendix A. The expressions for the strain components follow by substitution of the stress components into Hooke's law. The generalized stress-strain relations are:

$$\sigma_{kl} = C_{klmn}\varepsilon_{mn}, \quad (10)$$

and

$$\varepsilon_{kl} = S_{klmn}\sigma_{mn}, \quad (11)$$

where the C_{klmn} are the compliance and the S_{klmn} the stiffness coefficients. For materials with cubic symmetry, only three of the 81 components are independent. So $C_{11} = C_{1111} = C_{2222} = C_{3333}$, $C_{12} = C_{1122} = C_{2233}$, etc., and $C_{44} = C_{1212} = C_{2323}$, etc.; similar relations hold for S_{11} , S_{12} and S_{44} . The stress-strain relations can then be written in terms of Young's modulus E and Poisson ratio ν . Since

$$E = \frac{1}{S_{11}} = \frac{(C_{11} - C_{12})(C_{11} + 2C_{12})}{C_{11} + C_{12}}, \quad (12)$$

and

$$\nu = -ES_{12} = \frac{C_{12}}{C_{11} + C_{12}}, \quad (13)$$

then

$$\sigma_{ij} = \frac{E}{1+\nu} \varepsilon_{ij} + \frac{\nu E}{(1+\nu)(1-2\nu)} \delta_{ij} \varepsilon_{kk}, \quad (14)$$

and

$$\varepsilon_{ij} = \frac{1}{E} [(1+\nu)\sigma_{ij} - \delta_{ij}\nu\sigma_{kk}]. \quad (15)$$

In this paper we define the hydrostatic and the biaxial strains as

$$\varepsilon_h = \varepsilon_{xx} + \varepsilon_{yy} + \varepsilon_{zz}, \quad (16)$$

and

$$\varepsilon_b = \varepsilon_{zz} - \frac{1}{2}(\varepsilon_{xx} + \varepsilon_{yy}), \quad (17)$$

respectively. These relations are introduced here because they represent important quantities used in the analysis of the electronic energy levels in a later section.

3. Strain distribution

We have calculated the strain distributions for a number of structures whose dimensions are given in Table 1. Calculations for pyramidal QDs, labeled PQD in Table 1, as well as truncated pyramidal dots, labeled TPQD in Table 1, have been carried out. We consider first structure PQD3 in Table 1; this type of structure has been extensively studied and reported on in the literature. Fig. 2 shows the strain tensor components ε_{xx} and ε_{zz} for structure PQD3, plotted as functions of position along the z -axis. The shear strain components, ε_{xy} , ε_{yz} , and ε_{xz} are negligible in the dot and barrier materials; they could, however, be appreciable at the interfaces [4]. By symmetry, the component $\varepsilon_{xx} = \varepsilon_{yy}$. In a thin substrate region below the dot,

the GaAs lattice experiences a tensile (positive ε_{xx}) strain in the x - y plane and a compressive (negative ε_{zz}) strain in the z direction. In this case, the dot is forcing the substrate lattice constant to be that of InAs ($a_{\text{InAs}} = 6.05 \text{ \AA}$). In the base region of the dot, the situation is reversed. Here, ε_{zz} is positive and ε_{xx} negative because the substrate now attempts to force the dot lattice constant to be that of GaAs ($a_{\text{GaAs}} = 5.65 \text{ \AA}$). With increasing height within the dot, ε_{zz} changes its sign, becoming negative at the top of the pyramid. At the top of the pyramid, the dominant forces acting on the dot originate from the GaAs matrix at the sides, causing a compressive strain (negative ε_{zz}) along the z direction and a tensile strain (positive ε_{xx}) in the x - y plane. Fig. 3 is a plot of the ε_{xx} and ε_{zz} components along the x -axis for structure PQD3. Within the dot, both ε_{xx} and ε_{zz} are negative, implying the existence of a region of hydrostatic compression. The ε_{xx} , ε_{yy} , and ε_{zz} components of the strain tensor are plotted in Figs. 4(a), (b), and (c) in the x - z plane.

The hydrostatic and biaxial components of the strain for structure PQD3 are plotted as functions of position along the z -axis in Fig. 5. The hydrostatic strain is compressive within the dot and in the surrounding barrier material. The interior of the quantum dot exhibits a nearly homogeneous hydrostatic strain, while the barrier experiences a small hydrostatic strain. This is because GaAs is stiffer than InAs. The biaxial strain tends to be negative in the barrier and positive in the dot, and it is zero near the center of the dot. In this region, the strain is entirely hydrostatic in character. Fig. 5 suggests that a significant transfer of biaxial strain to the barrier takes place.

Table 1
Dimensions of single (In,Ga)As/GaAs quantum-dot structures used for computations

Structure	Base width B (nm)	Pyramid height H (nm)	Truncation factor t	Truncated pyramid height h (nm)
PQD1	12	3		
PQD2	12	4		
PQD3	12	6		
PQD4	16	6		
PQD5	20	6		
TPQD1	13.8	4.6	0.25	1.15
TPQD2	13.8	4.6	0.50	2.30
TPQD3	13.8	4.6	0.75	3.45
TPQD4	19.7	4.7	0.64	3.00

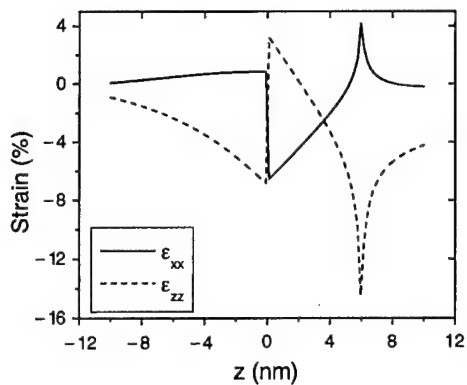


Fig. 2. Strain tensor components ε_{xx} and ε_{zz} for structure PQD3 plotted along the z -axis.

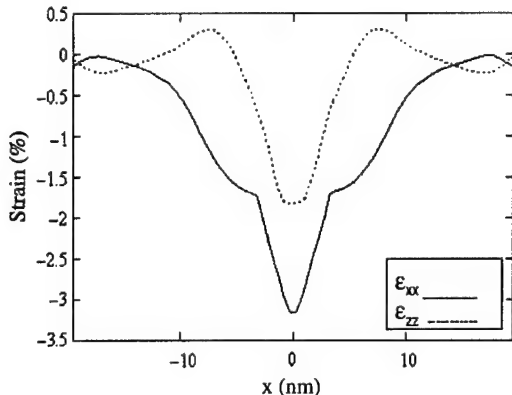


Fig. 3. Strain tensor components ε_{xx} and ε_{zz} for structure PQD3 plotted along the x -axis.

We have studied strain relaxation in the pyramidal InAs/GaAs QDs for the different structures labeled PQD(1–5) in Table 1. We compare the strain distributions in the x – z plane for dots of different base widths ($B_1 = 12$ nm for PQD3, $B_2 = 16$ nm for PQD4, and $B_3 = 20$ nm for PQD5) but the same height ($H = 6$ nm) in Fig. 6. We note that for dots with small base widths, the strain components change sign from the base region of the dot to the apex more rapidly than for dots with large base widths. For example, in structure PQD5, the strain components ε_{xx} and ε_{yy} are negative inside the dot, while in structure PQD3, they change sign from negative at the base of the dot to positive at the apex of the dot. The strain component ε_{zz} changes rapidly from positive to negative values along the

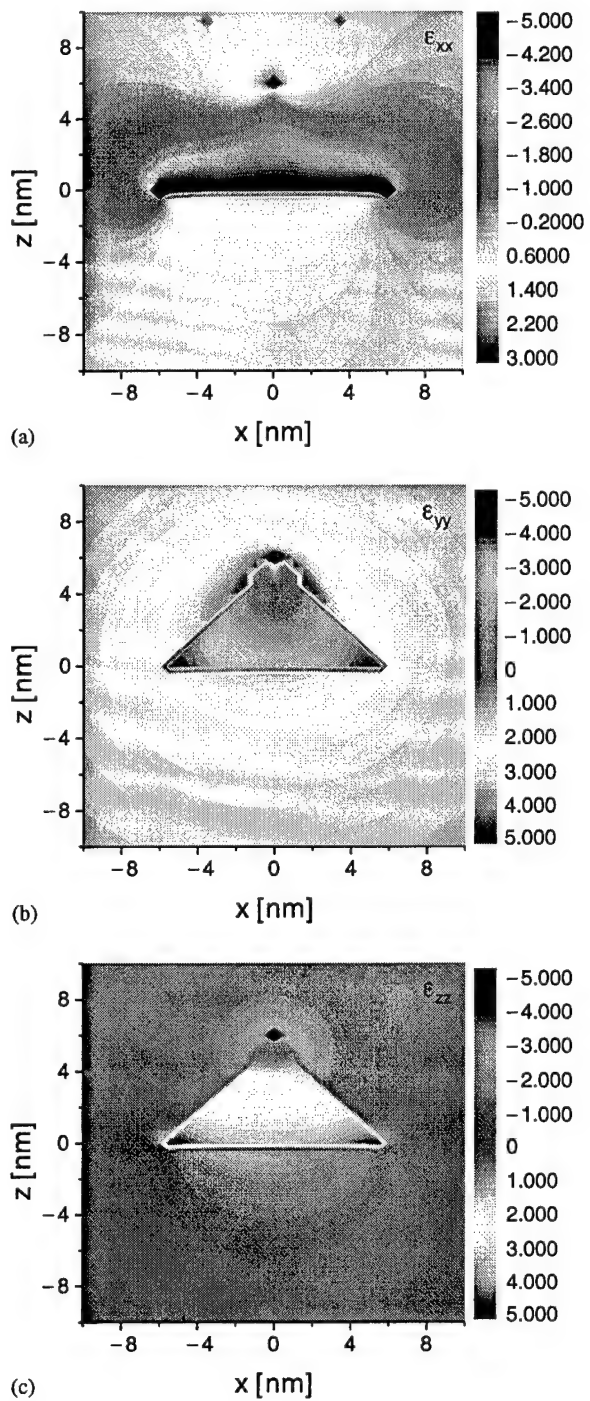


Fig. 4. Strain tensor components for structure PQD3 in the x – z plane: (a) ε_{xx} , (b) ε_{yy} , (c) ε_{zz} (strain expressed in %).

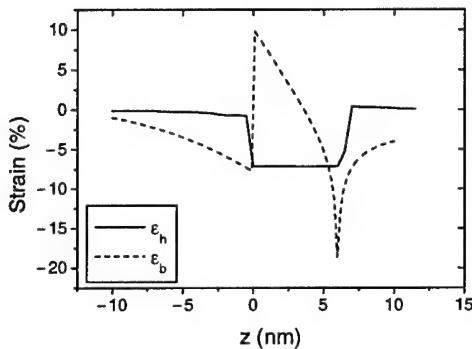


Fig. 5. The hydrostatic ϵ_h , and biaxial ϵ_b components of the strain for structure PQD3 plotted along the z -axis.

z -axis in structure PQD3, but is mostly tensile inside structure PQD5. The electronic structure of the dots is also expected to have such a strong dependence on the base lengths, as we will discuss in Section 4.

Fig. 7 illustrates the strain relaxation pattern for InAs dots of the same base width ($B = 12$ nm) but different heights ($H_1 = 3$ nm for PQD1, $H_2 = 4$ nm for PQD2, and $H_3 = 6$ nm for PQD3). This comparison suggests that the strain-modified electronic energy structure is likely not to be as sensitive to variations in the height of the dot as it is to changes in the base width of the dot. Extraordinarily tall dots have large hydrostatic strains near their centers. This increases the band gap inside the islands, partially compensating for the change in confinement potential.

Calculations indicate that when InAs self-assembled pyramidal dots are buried under a GaAs overlayer, significant tensile stress is induced at the top of the dot; the stress at the edges of the dot, on the other hand, is weak and compressive. This is in contrast to surface dots, where stress relaxation occurs at the island tops but is concentrated at the edges [10]. It should be noted that the stress component σ_{zz} (at the $x = 0$ plane) is compressive (negative) in embedded dots whereas it is tensile (positive) in uncovered ones. The strain distribution maps calculated here for pyramidal InAs dots are in reasonably good agreement with published results obtained by calculations based on atomistic methods [4,24]. The agreement is surprisingly good considering the computational simplifications introduced in the present work.

We have extended the analytical procedure to calculating strain distributions of truncated InAs pyramidal

dots such as that shown in the transmission electron microscope (TEM) image of Fig. 8. The structure in this figure was grown by molecular beam epitaxy on a (001) GaAs substrate. From the substrate up, the structure consists nominally of a 250-nm-GaAs buffer layer; this is followed by five periods of InAs/GaAs quantum dots. The entire structure is capped with 27 nm of GaAs. The dot density, as determined by atomic force microscope, was about $4 \times 10^{10} \text{ cm}^{-2}$. The shape of the dots was determined from cross-sectional TEM studies. The TEM image clearly shows that the dots are coherent, with no observable dislocations. The dots could be discerned from their darker appearance due to the presence of Indium. The buried dots appear to be pyramids with truncated tops; their base and height were found to be $B = 13.8$ nm, and $h = 3.4$ nm, respectively. This corresponds to a truncation factor of $t = 0.75$ (structure TPQD3 in Table 1). This observation is consistent with previous reports [25]. We have calculated the strain tensor components, as well as the hydrostatic and the biaxial strain profiles for this structure. The results are shown in solid lines in Fig. 9. We mention that the analytical results obtained for structure TPQD3 are in very good agreement with those obtained for a similar structure, using finite element method, in Ref. [26].

For pyramidal dots of arbitrary truncation, general expressions for the stress tensor components can be derived. These expressions are given in the Appendix A for a uniformly lattice-mismatched InAs/GaAs dot. Calculations based on these expressions for truncated InAs/GaAs dots have been performed for structures TPQD(1–3) in Table 1. The specific truncation factors used are $t = 0.25, 0.50$, and 0.75 , respectively. For $t = 1$ we obtain the whole pyramidal geometry, while for $t = 0$, we merely reproduce results for the two-dimensional wetting layer alone.

There are several features that are common to all strain distributions for the structures studied. First, the magnitudes of the strain components are largest at the dot/matrix interface, particularly at the vertices. The strain is rapidly attenuated within the dot and in the matrix material immediately below the square base of the dot. It remains of similar form for each truncation since the base of the dot is unchanged. The hydrostatic strain is zero in the matrix material and proportional to ϵ_0 in the quantum dot, consistent with standard inclusion theory. The conduction band shift

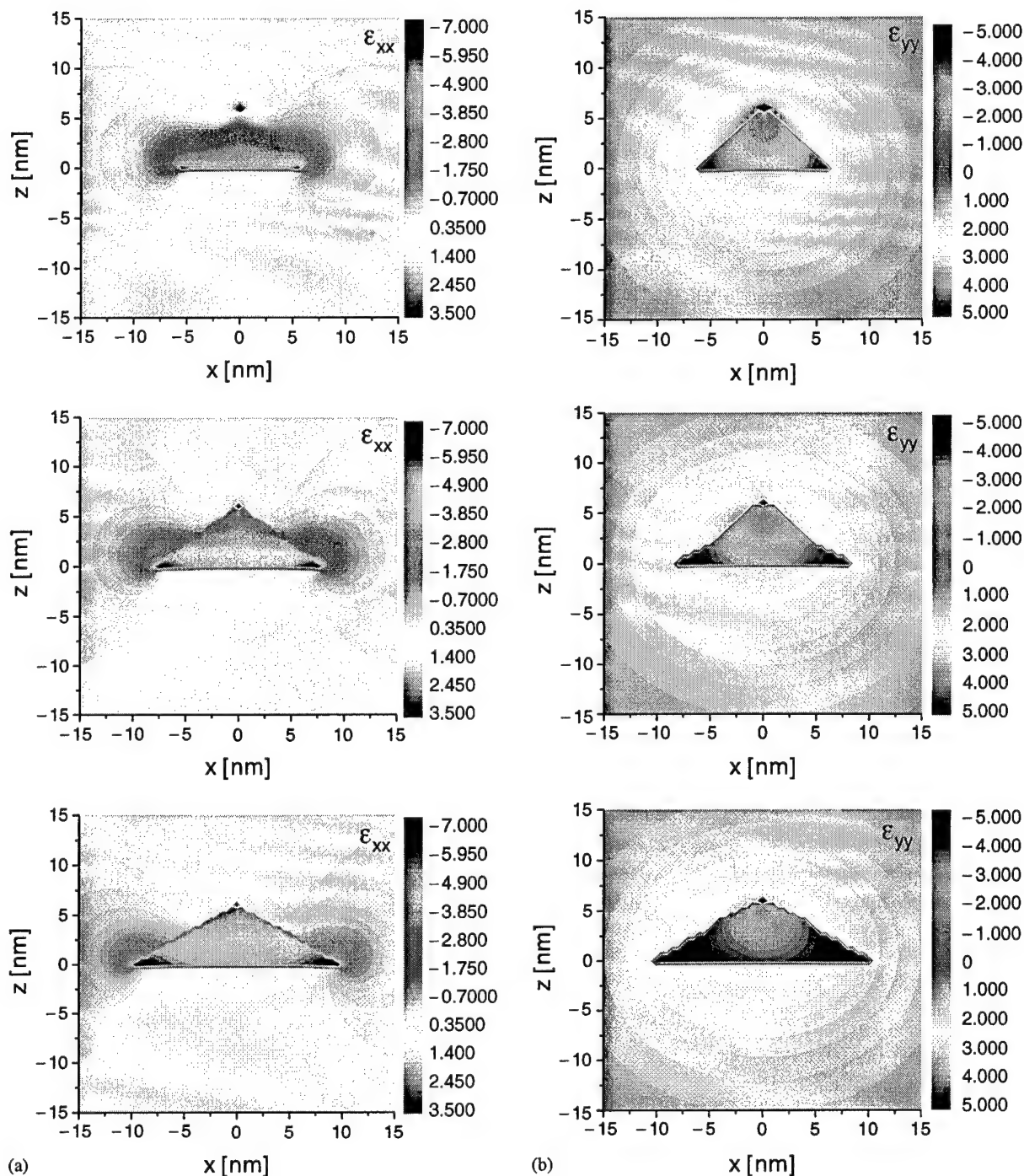


Fig. 6. Comparison of strain components for structures PQD(3-5), characterized by height $H = 6$ nm, but different base widths: $B_1 = 12$ nm (PQD3), $B_2 = 16$ nm (PQD4), and $B_3 = 20$ nm (PQD5): (a) ε_{xx} , (b) ε_{yy} , (c) ε_{zz} (strain expressed in %).

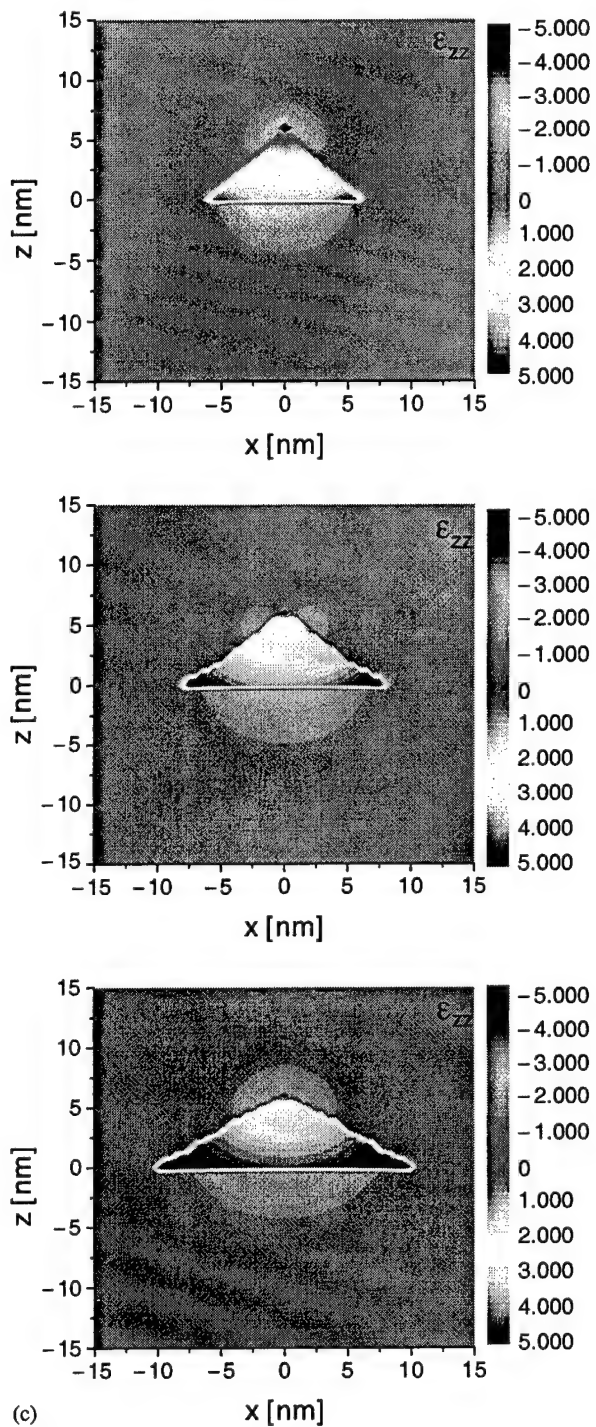


Fig. 6. (Continued.)

depends on the hydrostatic strain, so the conduction band shift is relatively constant within a dot of constant composition. Figs. 9(a) and (b) illustrate the ε_{xx} and ε_{zz} strain tensor components plotted along the z -axis for structures TPQD(1–3) of Table 1.

Our results, and those of others, indicate that the magnitudes of the strain components depend on the geometries of the dots. This is as it should be for both qualitative and quantitative reasons. Consider, for example, that the biaxial strain is very sensitive to truncation (see Fig. 9(c)); at the apex of the pyramid, the biaxial strain is negative, but becomes increasingly positive as the degree of truncation increases.

For structure TPQD4 we consider the case where the dot material is a ternary compound; in particular, we consider the case where the Indium composition is 23%, as determined from X-ray diffraction experiments. And as before, the shape and size of the dots are determined from cross-sectional high-resolution TEM observations. We have performed calculations to determine the strain tensor components for $\text{In}_{0.23}\text{Ga}_{0.77}\text{As}/\text{GaAs}$ dots. The strain distributions are depicted in Fig. 10 for structure TPQD4. The strain tensor components obtained here are used as input for the electronic band structure calculations discussed in the next section.

4. Electronic structure and optical transitions

The band structure of semiconductors is generally altered by the presence of strain, which changes the lattice constant and reduces the symmetry of the crystal. Strain modifies energy gaps and removes degeneracy. Here, we take account of the strain distributions discussed in the previous sections in calculating the electronic structure of dots in the envelope function approximation using an eight-band strain-dependent $\mathbf{k} \cdot \mathbf{p}$ Hamiltonian [27]. The eight-band $\mathbf{k} \cdot \mathbf{p}$ method represents an extension of the Luttinger–Kohn formalism, which describes coupling among the light-hole, heavy-hole and split-off valence bands to second order in \mathbf{k} , but is modified to include the linear coupling between the conduction and valence band states. This is necessary in order to correctly model conduction band non-parabolicity. A product of strain components and a deformation potential describes the general form of the strain-induced modification of the band

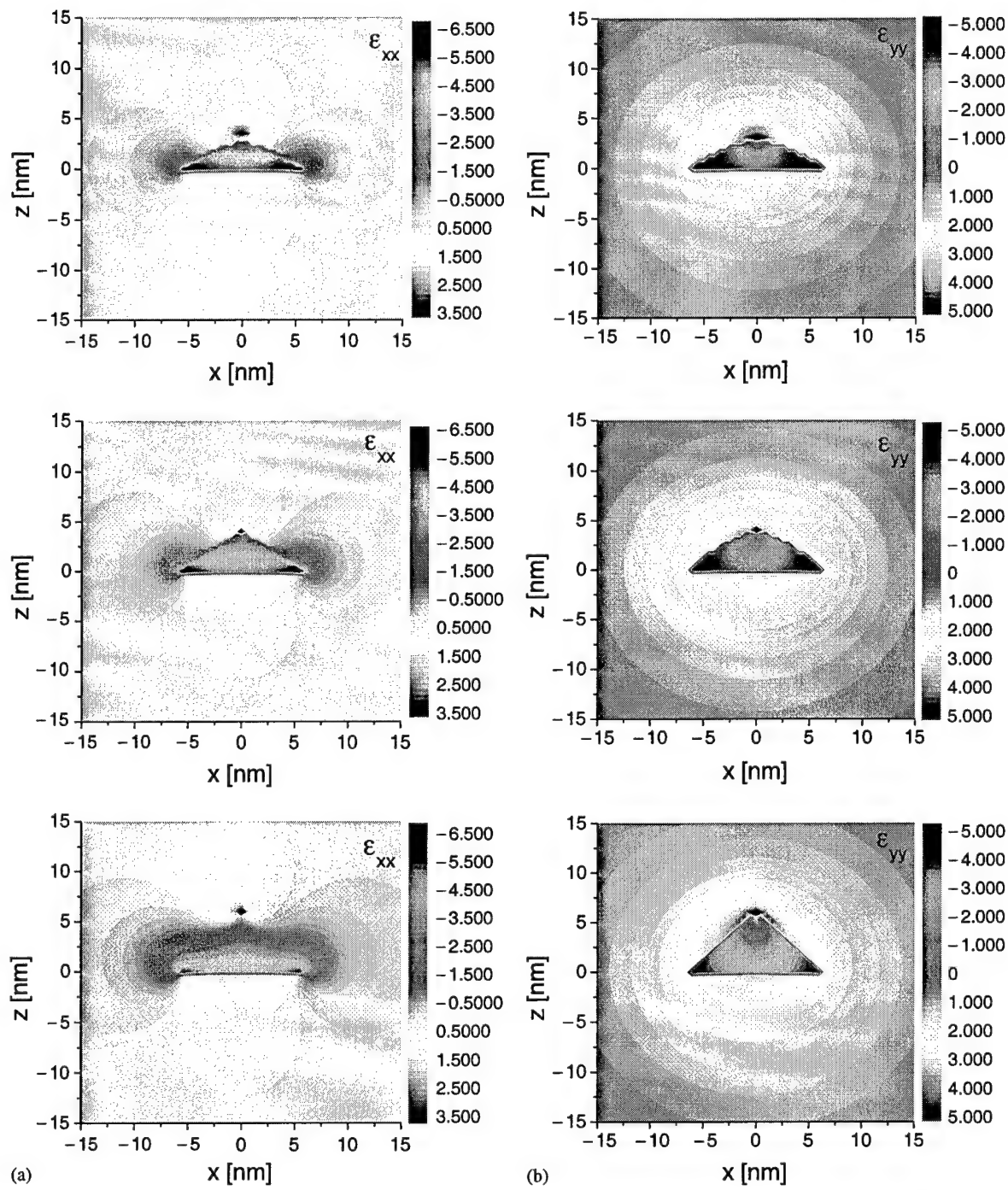


Fig. 7. Comparison of strain components for structures PQD(1–3), characterized by base width $B = 12$ nm, but different heights: $H_1 = 3$ nm (PQD1), $H_2 = 4$ nm (PQD2), and $H_3 = 6$ nm (PQD3): (a) ε_{xx} , (b) ε_{yy} , (c) ε_{zz} (strain expressed in %).

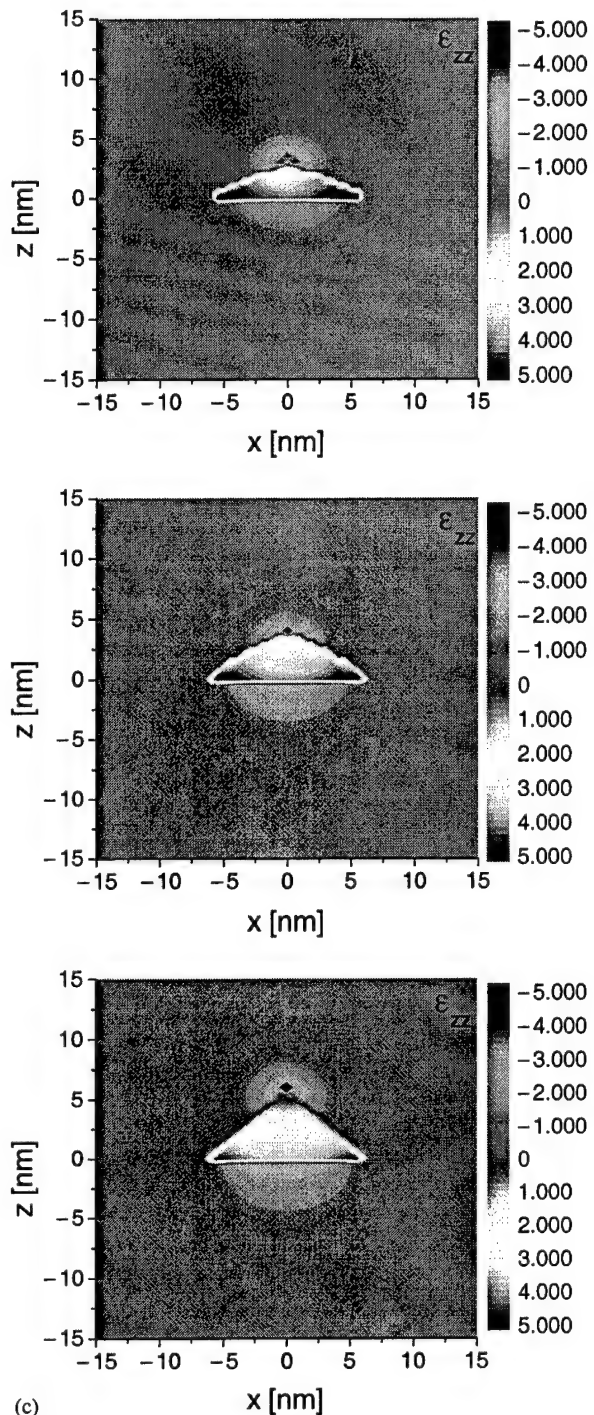


Fig. 7. (Continued.)

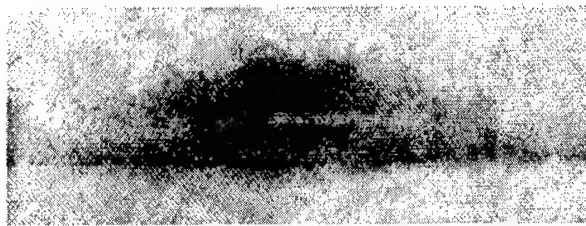


Fig. 8. Cross-sectional high-resolution transmission electron microscope image of InAs quantum dots in a GaAs matrix.

structure. Typical values of deformation potentials range from 1 to 10 eV [22]. These determine the amount of band structure modification and enter the calculations as material parameters given in Table 2. In our calculations, we neglect the lack of inversion symmetry in the zincblende structure and consequently ignore the small coupling of the conduction band to shear deformations. In the strain-dependent Hamiltonian, the non-diagonal terms containing shear components of the strain are non-zero in our geometries, except far away from the dot axis. However, since the diagonal shear strain term of the Hamiltonian decouples the heavy- and light-hole bands by approximately 100 meV, the correction of the non-diagonal terms in the Hamiltonian is small near the band-edge. The resultant Hamiltonian is a matrix that is diagonalized using the Lanczos algorithm developed in Refs. [28,29].

Some insight can be gleaned by examining the strain-induced modification to the band structure corresponding to structure PQD3 in Table 1. In the absence of strain, the confining potential for an electron (hole) is a square well formed by the difference in the absolute energy of the conduction (valence) band-edges in InAs and GaAs [30]. In the conduction band, the depth of the confining potential in this case is about 840 meV. For holes, the potential well is about 263 meV deep. However, because of strain, the confining potential for each carrier type is shifted. Since the strain varies with position, the confining potentials will also vary with position. The material parameters used in our computations are given in Table 2. Under these considerations, the conduction band can be given as

$$E_c(\varepsilon) = E_c^0 + \delta E_c(\varepsilon), \quad (18)$$

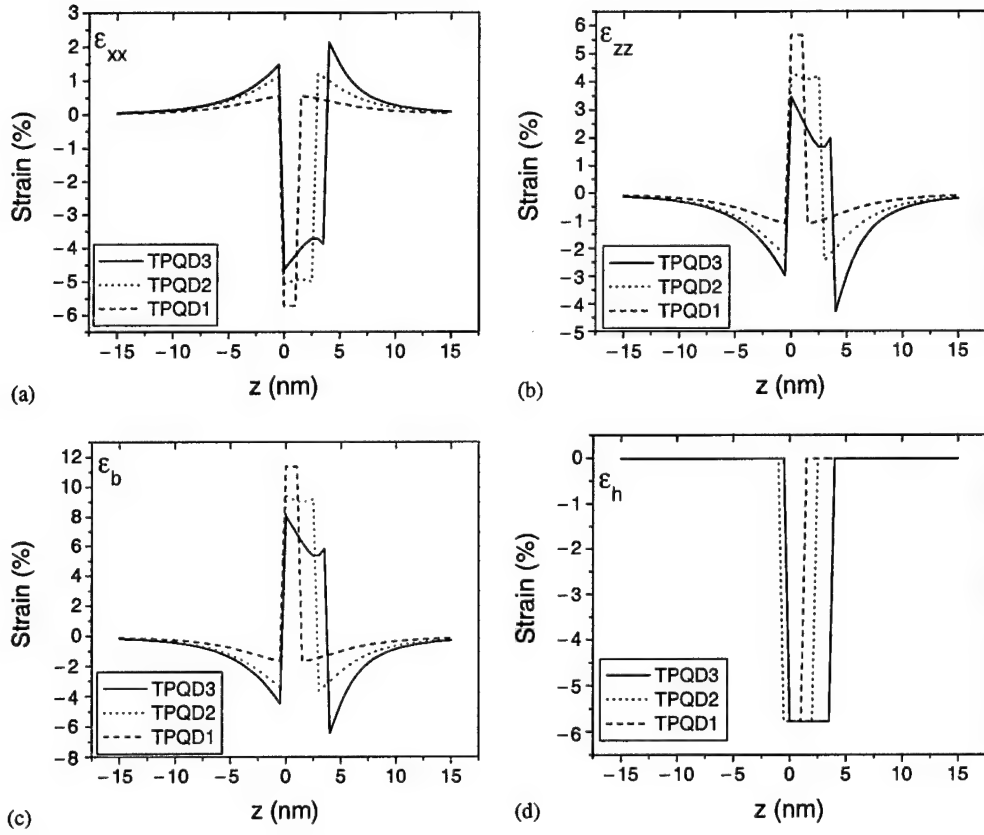


Fig. 9. Strain tensor components ϵ_{xx} and ϵ_{zz} along the z -axis for $t = 0.25$ (TPQD1), $t = 0.50$ (TPQD2), and $t = 0.75$ (TPQD3): (a) ϵ_{xx} , (b) ϵ_{zz} , (c) ϵ_b , and (d) ϵ_h .

where E_c^0 is the offset of the unstrained conduction band, which is

$$E_c^0 = E_{v,av}^0 + \frac{\Delta_0}{3} + E_g, \quad (19)$$

and δE_c is the strain-induced shift of the conduction band which is expressed as

$$\delta E_c(\epsilon) = a_c(\epsilon_{xx} + \epsilon_{yy} + \epsilon_{zz}). \quad (20)$$

In Eq. (19), Δ_0 is the spin-orbit splitting, E_g is the unstrained band gap, and $E_{v,av}^0$ is the unstrained average valence band-edge. The parameter a_c in Eq. (20) is the deformation potential for the conduction band.

The effect of strain on the valence band depends largely on the symmetry of the strain. The heavy- and light-hole energy bands, E_v^{hh} and E_v^{lh} , couple to the individual strain components via the relations [31]:

$$E_v^{hh} = E_{v,av}^0 + \frac{\Delta_0}{3} + \delta E_{v,h} - \frac{1}{2} \delta E_{v,b}, \quad (21)$$

and

$$E_v^{lh} = E_{v,av}^0 - \frac{\Delta_0}{6} + \delta E_{v,h} + \frac{1}{4} \delta E_{v,b} + \frac{1}{2} \sqrt{\Delta_0^2 + \Delta_0 \delta E_{v,b} + \frac{9}{4} (\delta E_{v,b})^2}, \quad (22)$$

where $\delta E_{v,h} = a_v \epsilon_h$, and $\delta E_{v,b} = b \epsilon_b$. The deformation potentials a_v and b are given in Table 2.

The dominant effect of the strain is that the dot experiences a large increase in its band gap due to the considerable hydrostatic pressure. The conduction band for structure PQD3 in Table 1 has a potential well that is 0.4 eV deep at the base of the dot, tapering off to a depth of about 0.27 eV at the apex. The valence band has a more complicated structure. If we could somehow turn off the strain, the holes would be confined to the InAs by a well that is only 85 meV deep. However, the presence of strain alters this considerably,

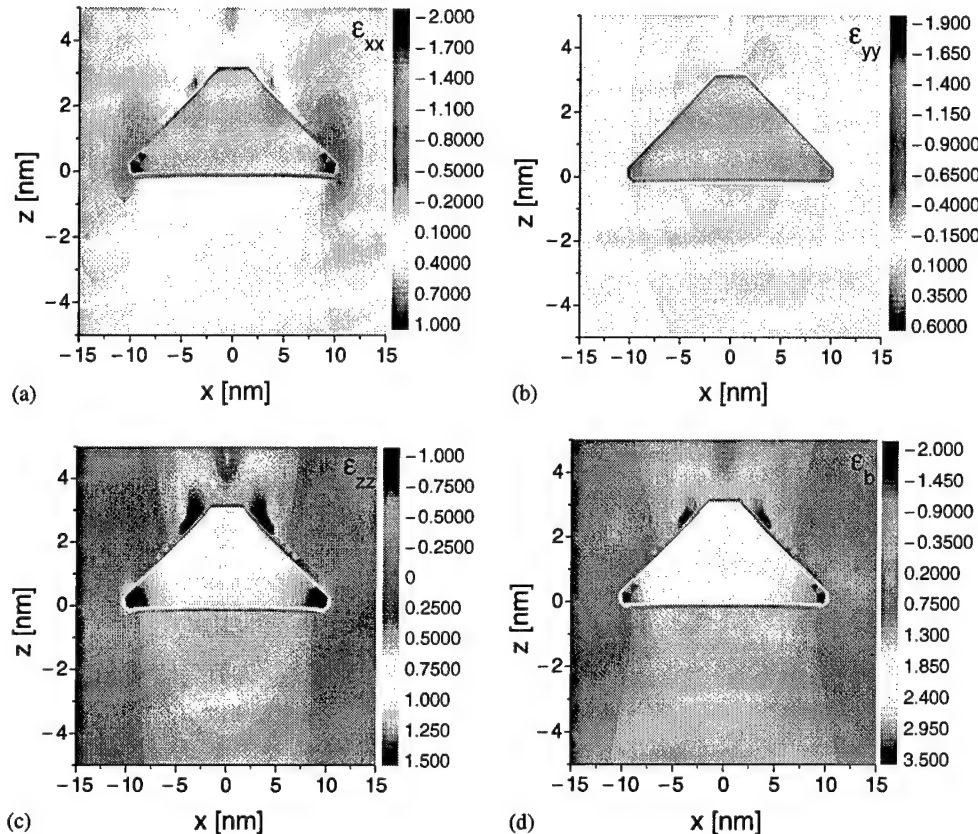


Fig. 10. Strain tensor components in the x - z plane for structure TPQD4: (a) ε_{xx} , (b) ε_{yy} , (c) ε_{zz} , and (d) ε_b (strain expressed in %).

Table 2
Material parameters used in calculations

Parameter	GaAs	InAs	$In_xGa_{1-x}As$
a (Å)	5.6503	6.0553	$(5.6503 + 0.405x)$ [32,39,40]
E_g (eV)	1.518	0.413	$(1.518 - 1.580x + 0.475x^2)$ [30,33,39,40] [$T = 6.4$ K]
E_g (eV)	1.424	0.324	$[0.324 + 0.7(1 - x) + 0.4(1 - x)^2]$ [39,40] [$T = 300$ K]
Δ_0 (eV)	0.340	0.380	$(0.340 - 0.093x + 0.133x^2)$ [30,38,39]
C_{11} (N/m ²)	11.88	8.33	$(11.88 - 3.55x)$ [32,33,39,40]
C_{12} (N/m ²)	5.38	4.53	$(5.38 - 0.85x)$ [32,33,39,40]
a_c (eV)	-8.013	-5.08	$(-8.013 + 2.933x)$ [30,33,39]
a_v (eV)	1.16	1.00	[30,33,39]
b (eV)	-1.7	-1.8	[30,33,39]
$E_{v,av}^0$ (eV)	-6.92	-6.747	$(-6.92 + 0.231x - 0.058x^2)$ [30,33,39]
m_e^*	$0.0667m_0$	$0.02226m_0$	$(0.0667 - 0.0419x - 0.00254x^2)$ [33,39]
E_p (eV)	25.7	22.2	$[(1.238 - 0.2095x)(1 - m_e/m_c)(3E_g(E_g + \Delta_0)/3E_g + 2\Delta_0)]$ [33,38]

and it, in fact, makes the dominant contribution to the hole confinement potential. A remarkable feature of the valence band is that it is peaked at the apex of the

dot and near the base. This is clearly evident in the energy band diagram presented along the z -axis for structure PQD3 in Fig. 11.

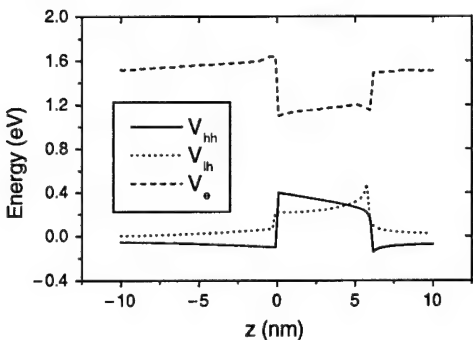


Fig. 11. Electron (V_e), heavy-hole (V_{hh}), and light-hole (V_{lh}) potential profiles for structure PQD3, plotted along the z -axis.

The confining potentials, inclusive of the effects of strain, are piecewise continuous functions of position. These potentials are shown in Fig. 11 for both electrons and holes. The split-off valence band is sufficiently far off in energy from the heavy- and light-hole band-edges, so it plays no role in the calculations. Note that the heavy- and light-hole confining potential wells are shown inverted. The anisotropic (biaxial) components of the strain in the dot and barrier reduce the symmetry of the conventional cubic unit cells, lifting the heavy- and light-hole degeneracy. The compressive strain in the barrier shifts the GaAs conduction band-edge slightly above the unstrained level of 1.52 eV. Note that in Fig. 11, the light-hole band-edge is higher in energy than the heavy-hole band-edge in the barrier, and at the apex of the pyramid. The heavy-hole band is the uppermost band at the base of the pyramid. The direction and magnitude of the splitting of the light- and heavy-hole bands—in the absence of appreciable shear strain components—is dependent solely on the magnitude and sign of the biaxial strain, ϵ_b . In those regions of the structure where the biaxial strain is negative, the light-hole band will be shifted upwards in energy and the heavy-hole band downwards; in those regions where the biaxial strain is positive, the heavy-hole band will be uppermost. When the biaxial strain is zero, the light- and heavy-hole bands are degenerate.

We show the electron confining potential in the x - z plane in Fig. 12(a) for structure PQD3. Here, the zero of energy is fixed at the GaAs level. The potential well for electrons has a depth of about 400 meV over much of the pyramid, deepening to about 450 meV at

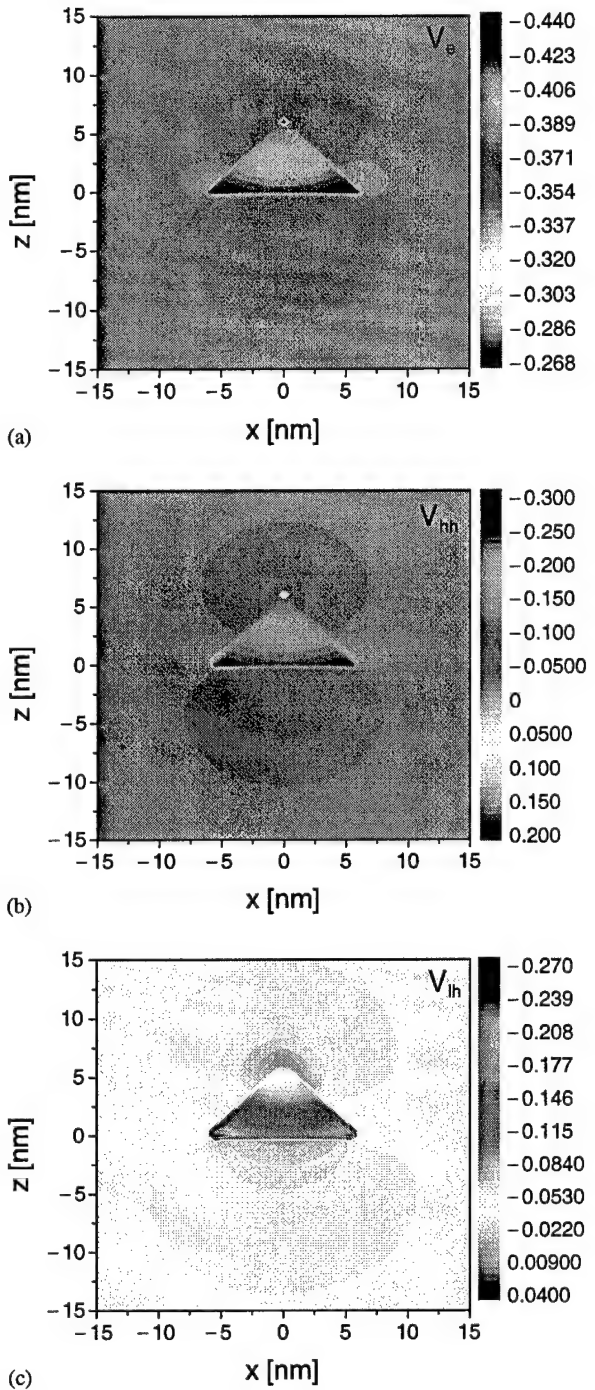


Fig. 12. Confining potential experienced by charge carriers in the x - z plane for structure PQD3 (negative values represent an attractive potential); (a) electrons, (b) heavy-holes, and (c) light-holes (potential expressed in eV).

the base. In the wetting layer, the potential is taken to be identical to the potential near to the base of the pyramid. The potential in the barrier is close to zero since the material here is GaAs. Fig. 12(b) shows the contour plot of the confining potential experienced by heavy-hole carriers. In the regions attractive to heavy-holes, the potential is negative. The potential inside the well has a positive gradient from the base towards the apex. Over this distance, the potential changes by several hundred meV. Because of this and the large effective mass for heavy-holes, one would expect charge localization near the base of the pyramid. The contour plot for the light-hole confining potential is shown in Fig. 12(c). This plot shows a slowly varying attractive potential in the barrier region above and below the pyramid. It reaches a minimum at the apex of the pyramid.

Several methods have been developed to calculate the electronic structure of the square-based pyramidal InAs dots [4,6,11]. Among these is the pseudopotential plane-wave approach used by Williamson et al. [32]. To calculate the energy levels and electron (or hole) wave functions we use an eight-band effective mass approach. The strain effect is included via deformation potential theory [33]. The bound energy levels are computed as functions of quantum-dot size. The bound states of the dot are found by numerically solving the Schrödinger equation, which in the effective mass approximation, can be written as

$$-\frac{\hbar^2}{2} \nabla \left(\frac{1}{m_i^*(r)} \right) \nabla \Psi_n(r) + V(r) \Psi_n(r) = E \Psi_n(r). \quad (23)$$

In this expression, $m_i^*(r)$ must be replaced by $m_{\text{InGaAs}}^*(r)$ inside the dot, and by $m_{\text{GaAs}}^*(r)$ in the matrix material; $V(r)$ is the three-dimensional confining potential. In the framework of the eight-band model, the wave function can be expanded as a linear combination of the basis functions, thus

$$\Psi_n(r) = \sum_{j=1}^8 F_{nj}(r) u_j(r) = \sum_{J, J_z} |J, J_z\rangle F_{J, J_z}(r), \quad (24)$$

where $u_j(r)$ has the periodicity of the crystal lattice and j is the band index. At the band-edges, these functions are characterized by symmetry arguments as eigenstates $|J, J_z\rangle$ of the Bloch angular momentum J .

The states $|J, J_z\rangle$ are the band-edge functions of the Bloch state space [34]. These wave functions are, for the s -like Γ_1 conduction band,

$$\left| \frac{1}{2}, \frac{1}{2} \right\rangle_c = |S\rangle | \uparrow \rangle \quad \text{and} \quad \left| \frac{1}{2}, -\frac{1}{2} \right\rangle_c = |S\rangle | \downarrow \rangle, \quad (25)$$

while for the p -like Γ_8 , Γ_7 valence bands, they can be written as [34]

$$\begin{aligned} \left| \frac{3}{2}, \frac{3}{2} \right\rangle_v &= \left(\frac{1}{\sqrt{2}} \right) (|x\rangle + i|y\rangle) | \uparrow \rangle, \\ \left| \frac{3}{2}, \frac{1}{2} \right\rangle_v &= \left(\frac{1}{\sqrt{6}} \right) (|x\rangle + i|y\rangle) | \downarrow \rangle \\ &\quad - \left(\sqrt{\frac{2}{3}} \right) |z\rangle | \uparrow \rangle, \\ \left| \frac{3}{2}, -\frac{1}{2} \right\rangle_v &= - \left(\frac{1}{\sqrt{6}} \right) (|x\rangle - i|y\rangle) | \uparrow \rangle \\ &\quad - \left(\sqrt{\frac{2}{3}} \right) |z\rangle | \downarrow \rangle, \\ \left| \frac{3}{2}, -\frac{3}{2} \right\rangle_v &= \left(\frac{1}{\sqrt{2}} \right) (|x\rangle - i|y\rangle) | \downarrow \rangle, \\ \left| \frac{1}{2}, \frac{1}{2} \right\rangle_v &= \left(\frac{1}{\sqrt{3}} \right) (|x\rangle + i|y\rangle) | \downarrow \rangle \\ &\quad + \left(\sqrt{\frac{1}{3}} \right) |z\rangle | \uparrow \rangle, \\ \left| \frac{1}{2}, -\frac{1}{2} \right\rangle_v &= - \left(\frac{1}{\sqrt{3}} \right) (|x\rangle - i|y\rangle) | \uparrow \rangle \\ &\quad + \left(\sqrt{\frac{1}{3}} \right) |z\rangle | \downarrow \rangle. \end{aligned} \quad (26)$$

We want to point out that it is generally known that the $\mathbf{k} \cdot \mathbf{p}$ method has some problems associated with it when applied to calculations involving nanostructures [33]. These difficulties include (i) the fixed number of Bloch functions (eight in the formalism used here), (ii) the restriction of the validity of the method to the Brillouin zone center, (iii) the use of the same Bloch functions, regardless of material and strain variations,

and (iv) the difficulty of choosing appropriate boundary conditions with associated matching criteria for the envelope functions across the heterointerfaces. In our calculations, we take into account the variation of mass parameters from their bulk values due to the strain-induced band deformations. The details of the guidelines used have been discussed by Burt [35].

The eigenvalues and eigenfunctions of Eq. (23) are obtained by invoking periodic boundary conditions, expanding $\Psi_n(r)$ in terms of normalized plane-wave states, and diagonalizing the resulting matrix. This approach, which has also been used by Cusack et al. [6], does not require matching of the wave functions across the boundary between the dot and the matrix materials. This makes the method applicable to arbitrary (position dependent) confining potentials. The only requirement on the boundary conditions is that the states do not significantly overlap for dots adjacent to each other.

In general, the number of confined states in a quantum dot depends on the size of the dot and on the thickness of the wetting layer. For the conduction band, there are usually only a few bound states. The energy spacing between the ground state and the first excited state in the conduction band typically ranges from about 60 to 95 meV for the dot-sizes considered in our work (see Fig. 13). We find that the valence-band states are more tightly confined because of the large hole effective mass. The energy spacing here ranges from a few meV to 30 meV.

In our calculations, we have neglected the Coulomb interaction energy. This energy largely depends on the value of the dielectric constant. As a result, dots of the same size can belong to different confinement regimes in materials with different dielectric constants. In III–V compounds, with a typical relative dielectric constant of ~ 13 , the bulk exciton radius is > 10 nm, causing a structural quantum dot of similar dimension and sufficiently deep potential to be in the strong confinement regime [22]. Because of this, additional binding energy from the Coulomb effect is negligible since the dots are already in the strong confinement regime. In any case, the Coulomb interaction energy is small compared to the separation of the ground state from the first excited state for both electrons and holes.

In Fig. 13, we show the calculated electron and hole energy level dependence on pyramid base length. The electron (hole) levels are plotted relative to the

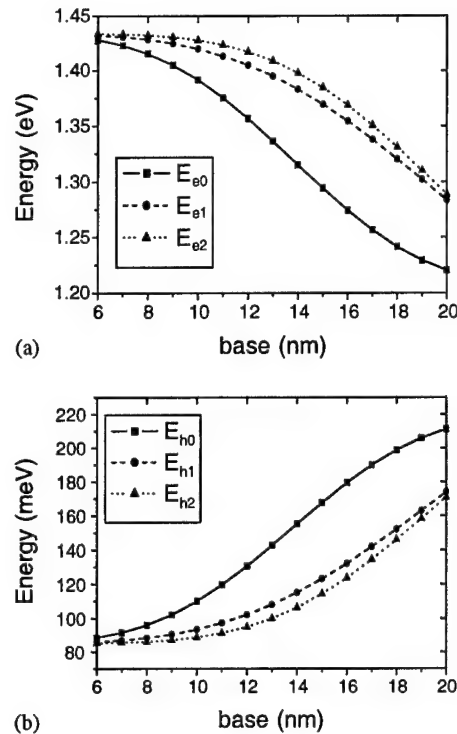


Fig. 13. (a) Electron and (b) hole quantum-dot energy levels (ground state and first two excited states), displayed as a function of dot base size.

unstrained GaAs conduction (valence) band-edge. For dot base dimensions smaller than ~ 6 nm, no bound electron states are predicted. Beyond 6 nm, a few states are predicted in the conduction band. And as stated earlier, many states are predicted in the valence band. This is due to the large effective mass associated with the holes and to the nature of the light-hole confining potential whose smoothly varying form leads to a quasi-continuum of tenuously bound states.

We have also determined the envelope functions for the first few confined states in the dot. Fig. 14(a), for example, shows the modulus-squared envelope function for the E_{e0} state for structure PQD3; this function is plotted in the y – z plane, cutting through the pyramid and the wetting layer. The relatively isotropic character of the confining potential for electrons, coupled with the small effective mass, results in a state that permeates throughout the dot and penetrates into the sides of the pyramid. Fig. 14(b) is the hole envelope function in the y – z plane for the state E_{h0} . Unlike the ground state in the conduction band, the hole ground

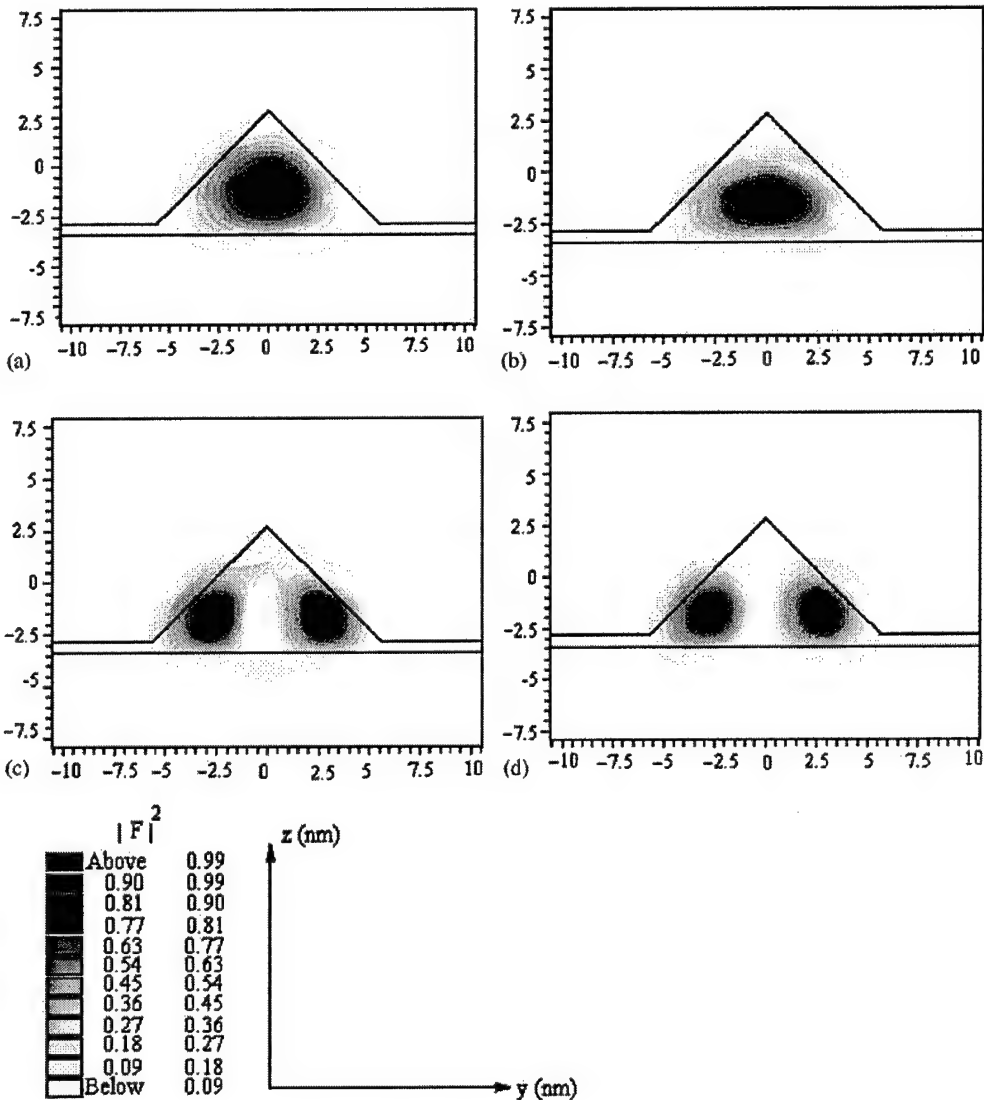


Fig. 14. The squared absolute magnitude of the envelope function for structure PQD3 across the y - z plane for energy levels: (a) E_{e0} , (b) E_{h0} , (c) E_{h1} , (d) E_{h2} .

state is confined to the base of the dot. In Fig. 14(c) and (d), we show the envelope functions for the hole excited states E_{h1} and E_{h2} .

The calculated transition energies for the ground state, $E_{e0} \rightarrow E_{h0}$, and for the first $E_{e1} \rightarrow E_{h1}$, and second $E_{e2} \rightarrow E_{h2}$ excited states for pyramids of various base dimensions are shown in Fig. 15(a). From Fig. 15(a), the calculated fundamental transition energy for a pyramid with a base length of 16 nm is 1.10 eV. This value is in good agreement with the experimen-

tally determined transition peak at 1.098 eV shown in Fig. 15(b). The same good agreement is found between the calculated and measured peak luminescence energy values for a 20-nm-base pyramidal quantum dot; the measured experimental data is shown in Fig. 15(c).

The energy splitting between the ground state and first excited hole state of 30 meV in Fig. 15(b) is in good agreement with a recent experimental study of the sub-level structure which measured a difference

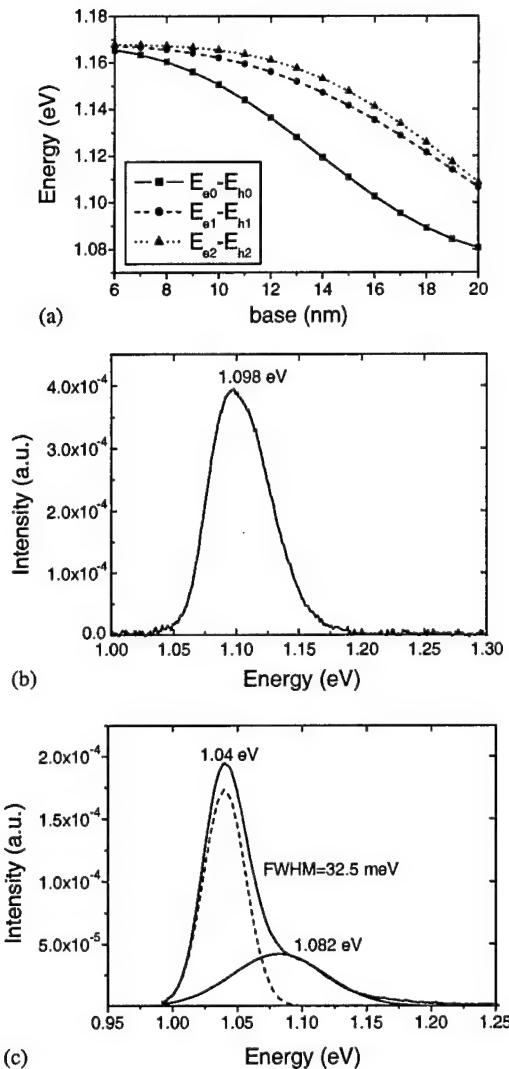


Fig. 15. (a) Calculated transition energies for pyramidal QDs: $E_{e0}-E_{h0}$, $E_{e1}-E_{h1}$, and $E_{e2}-E_{h2}$, as functions of QD base width; (b) Fundamental ($E_{e0}-E_{h0}$) transition energy measured by PL for a dot of base $B=16$ nm; and (c) for a dot of base width $B=20$ nm.

of approximately 27 meV [36]. The $E_{e0} \rightarrow E_{h0}$ transition is the dominant excitation in all of the structures studied.

We now consider the computation of the electronic energy levels in truncated pyramidal quantum dots. The basic approach is similar to what has already been discussed in this paper. For truncation factors ranging from 0.25 to 0.75, we show the confining potentials for electrons and holes in Fig. 16. The

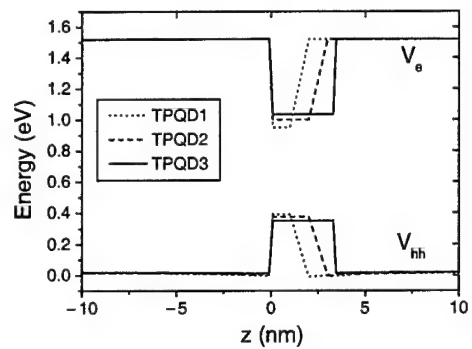


Fig. 16. Confining potentials for electrons and heavy-holes, along z -axis, for structures TPQD(1-3) with truncation factors: $t = 0.25$ (TPQD1), $t = 0.50$ (TPQD2), and $t = 0.75$ (TPQD3).

bound states are determined by numerically solving the Schrödinger equation within the context of approximations similar to those used in the ideal pyramid case. The calculated energy levels for the ground state and two excited states in the conduction, as well as the valence bands are shown in Fig. 17 for a range of truncation factors. As a specific example, we calculated the energy levels for structure TPQD3, whose dimensions are given in Table 1; the TEM micrograph of this structure was shown in Fig. 8. The first three confined electron energy levels, measured with respect to the unstrained GaAs conduction band-edge, are $E_{e0} = 1.404$ eV, $E_{e1} = 1.426$ eV, and $E_{e2} = 1.428$ eV. In the valence band, the corresponding heavy-hole levels—again measured with respect to the unstrained GaAs valence band-edge—are $E_{h0} = 328.79$ meV, $E_{h1} = 343.88$ meV, and $E_{h2} = 345.74$ meV. The transition energies, for the allowed transitions, are shown in Fig. 18(a); the fundamental transition, $E_{e0} \rightarrow E_{h0}$, is at 1.076 eV. This energy is in good agreement with the experimentally determined peak of 1.08 eV for the photoluminescence emission spectrum shown in Fig. 18(b) for structure TPQD3. The photoluminescence measurements were carried out using an Ar^+ ion laser ($\lambda = 488$ nm) as an excitation source. The emitted radiation was detected with a liquid- N_2 -cooled Ge detector.

In devices such as near-infrared lasers and mid-infrared detectors, the preferred medium in the active region is often an $(\text{In},\text{Ga})\text{As}/\text{GaAs}$, rather than an InAs/GaAs quantum-dot superlattice. In this case, it becomes necessary to perform the energy level

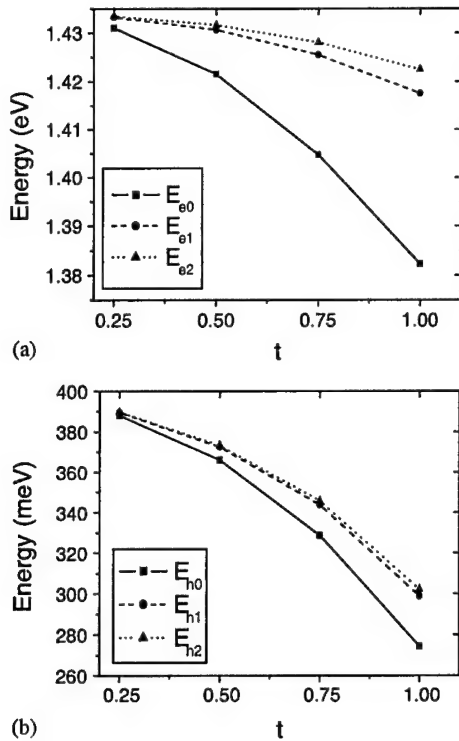


Fig. 17. Ground state and first two excited states for electrons and heavy-holes for structures TPQD(1–3) with truncation factors: $t = 0.25–0.75$.

calculations for (In,Ga)As dots. We have performed such calculations for truncated pyramidal $\text{In}_{0.23}\text{Ga}_{0.77}\text{As}$ dots. The parameters used in the calculations are given in Table 2. For illustrative purposes, we have used the truncated structure TPQD4 in Table 1. The fundamental transition energy, $E_{e0} \rightarrow E_{h0}$, for such a structure is calculated to be 1.126 eV. In the conduction band, the electron ground state of such a dot is separated by about 107 meV from the first excited state. These computed values are in good agreement with the photoluminescence and infrared absorption data obtained at 300 K [37].

5. Conclusions

The relaxation of strain and its residual component in lattice-mismatched epitaxy is responsible for the self-organization of quantum dots in the Stranski–Krastanow crystal growth mode. Beginning

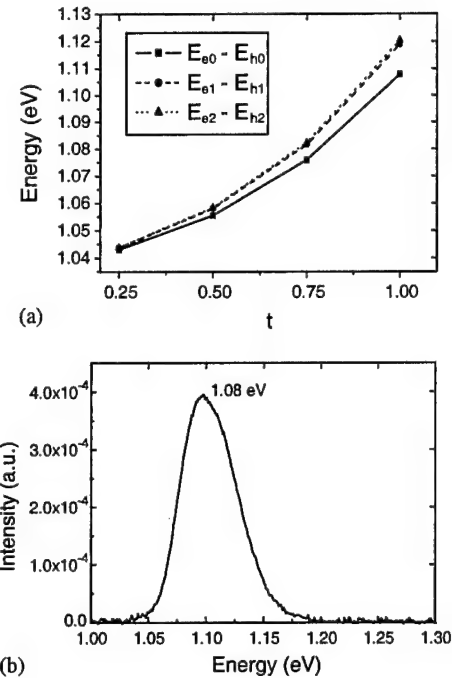


Fig. 18. Ground state and first excited state transition energies for structures TPQD(1–3) with truncation factors: $t = 0.25–0.75$: (a) calculated, (b) measured.

from this premise, we have calculated the strain distributions in pyramidal and truncated pyramidal (In,Ga)As/GaAs quantum dots using a method based on Eshelby's inclusion theory of continuum elasticity. It is found that the hydrostatic component of the strain is mostly confined within the dots, while the biaxial strain is transferred from the dot to the barrier material. By taking into account the influence of the strain on the band gap of the dots, we have solved the three-dimensional, effective mass, single-particle Schrödinger equation for the electronic energy levels in the dot. We find that strain plays a major role in the energy structure of the quantum dots. For the pyramidal geometry considered here, the electronic energy levels are also a sensitive function of the base length.

The results of our calculations are in good agreement with those reported in the literature, even though our method is considerably simpler than those used by others [4,20]. For the fundamental transition of a ground state electron in the conduction band recombining with a hole in its ground state in the

valence band, we find that our experimental results also agree with calculations.

In summary, we have developed a simple method for rapidly calculating strain in embedded quantum dots. The method allows one to determine the interdependence of strain on shape, and by extension, the effects of strain on confined energy levels in quantum dots.

Acknowledgements

This work was supported by the Army Research Office, Research Triangle Park, NC, and by the Army Research Laboratory, Adelphi, MD.

Appendix A

This section gives the more general mathematical expressions for the stress distributions inside pyramidal InAs quantum dots of different degrees of truncation. The expressions are obtained by integrating Eq. (6). They are given as functions of the space coordinate z , in the growth direction. The strain components follow immediately from Hooke's law, as given in Eq. (15). The following definitions are used in the expressions: the pyramid base width is $B = 2a$; the height, in the absence of truncation, is H ; the parameter t is the degree of truncation; and h is the height of a truncated pyramid. The stress component σ_{xx} , for example, is written as a summation over three terms:

$$\sigma_{xx} = \frac{h}{a^2 + h^2} \frac{E\varepsilon_0}{4\pi(1-\nu)} \times [\sigma'_{xx(1)} + \sigma'_{xx(2)} + \sigma'_{xx(3)}], \quad (\text{A.1})$$

where the terms $\sigma'_{xx(1)}$, $\sigma'_{xx(2)}$, and $\sigma'_{xx(3)}$ are given as

$$\sigma'_{xx(1)} = \frac{4a^2}{\sqrt{2a^2 + h^2}} \left\{ \ln \left[\frac{-2a^2(1-t) - h(z-ht)}{\sqrt{2a^2 + h^2}} \right] + \sqrt{2a^2(1-t)^2 + (z-ht)^2} \right. \\ \left. - \ln \left[\frac{-2a^2 - hz}{\sqrt{2a^2 + h^2}} + \sqrt{2a^2 + z^2} \right] \right\}. \quad (\text{A.2})$$

$$\sigma'_{xx(2)} = 2h \left\{ \tan^{-1} \left[\frac{-(z-ht)}{\sqrt{2a^2(1-t)^2 + (z-ht)^2}} \right] - \tan^{-1} \left[\frac{(z-ht)}{\sqrt{2a^2(1-t)^2 + (z-ht)^2}} \right] \right. \\ \left. + \tan^{-1} \left[\frac{z}{\sqrt{2a^2 + z^2}} \right] - \tan^{-1} \left[\frac{-z}{\sqrt{2a^2 + z^2}} \right] \right\}, \quad (\text{A.3})$$

and

$$\sigma'_{xx(3)} = a \ln \left\{ [a(1-t) + \sqrt{2a^2(1-t)^2 + (z-ht)^2}] \right. \\ \times \left[2a^2 \left(1 - \frac{z}{h} \right)^2 - a + \sqrt{2a^2 + z^2} \right] \\ \times 2a^2 \left(1 - \frac{z}{h} \right)^2 (-a + \sqrt{2a^2 + z^2}) \left. \right\} \\ - a \ln \left\{ [-a(1-t) + \sqrt{2a^2(1-t)^2 + (z-ht)^2}] \right. \\ \times \left[2a^2 \left(1 - \frac{z}{h} \right)^2 + a + \sqrt{2a^2 + z^2} \right] \\ \times 2a^2 \left(1 - \frac{z}{h} \right)^2 (a + \sqrt{2a^2 + z^2}) \left. \right\}. \quad (\text{A.4})$$

Similarly, for σ_{yy} we derive the following relations along the z -axis:

$$\sigma_{yy} = \frac{h}{a^2 + h^2} \frac{E\varepsilon_0}{4\pi(1-\nu)} [\sigma'_{yy(1)} + \sigma'_{yy(2)} + \sigma'_{yy(3)}], \quad (\text{A.5})$$

with $\sigma'_{yy(1)}$, $\sigma'_{yy(2)}$, and $\sigma'_{yy(3)}$ given as

$$\sigma'_{yy(1)} = \frac{4a^2}{\sqrt{2a^2 + h^2}} \left\{ \ln \left[\frac{-2a^2(1-t) - h(z-ht)}{\sqrt{2a^2 + h^2}} \right] + \sqrt{2a^2(1-t)^2 + (z-ht)^2} \right. \\ \left. - \ln \left[\frac{-2a^2 - hz}{\sqrt{2a^2 + h^2}} + \sqrt{2a^2 + z^2} \right] \right\}, \quad (\text{A.6})$$

$$\begin{aligned}\sigma'_{yy(2)} = & 2h \left\{ \tan^{-1} \left[\frac{-(z - ht)}{\sqrt{2a^2(1-t)^2 + (z - ht)^2}} \right] \right. \\ & - \tan^{-1} \left[\frac{(z - ht)}{\sqrt{2a^2(1-t)^2 + (z - ht)^2}} \right] \\ & \left. + \tan^{-1} \left[\frac{z}{\sqrt{2a^2 + z^2}} \right] - \tan^{-1} \left[\frac{-z}{\sqrt{2a^2 + z^2}} \right] \right\},\end{aligned}\quad (A.7)$$

$$\begin{aligned}\sigma'_{yy(3)} = & a \ln \left\{ [a(1-t) + \sqrt{2a^2(1-t)^2 + (z - ht)^2}] \right. \\ & \times \left[2a^2 \left(1 - \frac{z}{h} \right)^2 - a + \sqrt{2a^2 + z^2} \right] \\ & \times 2a^2 \left(1 - \frac{z}{h} \right)^2 (-a + \sqrt{2a^2 + z^2}) \Big\} \\ & - a \ln \left\{ [-a(1-t) + \sqrt{2a^2(1-t)^2 + (z - ht)^2}] \right. \\ & \times \left[2a^2 \left(1 - \frac{z}{h} \right)^2 + a + \sqrt{2a^2 + z^2} \right] \\ & \times 2a^2 \left(1 - \frac{z}{h} \right)^2 (a + \sqrt{2a^2 + z^2}) \Big\}.\end{aligned}\quad (A.8)$$

The other stress component, σ_{zz} , follows from:

$$\sigma_{zz} = \frac{2E\epsilon_0}{(1-\nu)} - (\sigma_{xx} + \sigma_{yy}). \quad (A.9)$$

References

- [1] A. Harvey, H. Davock, A. Dunbar, U. Bangert, P.J. Goodhew, *J. Phys. D: Appl. Phys.* 34 (2001) 636.
- [2] D. Leonard, K. Pond, P.M. Petroff, *Phys. Rev. B* 50 (1994) 11689.
- [3] E.P. O'Reilly, *Semicond. Sci. Technol.* 4 (1989) 121.
- [4] M. Grundmann, O. Stier, D. Bimberg, *Phys. Rev. B* 52 (1995) 11969.
- [5] T. Benabbas, P. François, Y. Androussi, A. Lefebvre, *J. Appl. Phys.* 80 (1996) 2763.
- [6] M.A. Cusack, P.R. Briddon, M. Jaros, *Phys. Rev. B* 54 (1996) R2300.
- [7] Y. Kikuchi, H. Sugii, K. Shintani, *J. Appl. Phys.* 89 (2001) 1191.
- [8] S. Christiansen, M. Albrecht, H.P. Strunk, H.J. Maier, *Appl. Phys. Lett.* 64 (1994) 3617.
- [9] L. De Caro, L. Tapfer, *Phys. Rev. B* 49 (1994) 11127.
- [10] D.A. Faux, S.G. Howells, U. Bangert, A.J. Harvey, *Appl. Phys. Lett.* 64 (1994) 1271.
- [11] A.H. Harker, K. Pinardi, S.C. Jain, A. Atkinson, R. Bullough, *Philos. Mag. A* 71 (1995) 871.
- [12] P.K. Banerjee, *Boundary Element Methods in Engineering*, McGraw-Hill, London, 1994.
- [13] J.R. Downes, D.A. Faux, E.P. O'Reilly, *J. Appl. Phys.* 81 (1997) 6700.
- [14] J.D. Eshelby, *Proc. R. Soc. London Ser. A* 241 (1957) 376.
- [15] T. Benabbas, Y. Androussi, A. Lefebvre, *J. Appl. Phys.* 86 (1999) 1945.
- [16] A.D. Andreev, J.R. Downes, D.A. Faux, E.P. O'Reilly, *J. Appl. Phys.* 86 (1999) 297.
- [17] O. Brandt, K. Ploog, R. Bierwolf, M. Hosenstein, *Phys. Rev. Lett.* 68 (1992) 1339.
- [18] D.A. Faux, G. Jones, E.P. O'Reilly, *Modell. Simul. Mat. Sci. Eng.* 2 (1994) 9.
- [19] D.A. Faux, J. Haigh, *J. Phys.: Condens. Mater* 2 (1990) 10 289.
- [20] C. Pryor, J. Kim, L.W. Wang, J. Williamson, A. Zunger, *J. Appl. Phys.* 83 (1998) 2548.
- [21] J. Kim, L.W. Wang, A. Zunger, *Phys. Rev. B* 57 (1998) R9408.
- [22] D. Bimberg, M. Grundmann, N.N. Ledentsov, *Quantum Dot Heterostructures*, Wiley, UK, 1998.
- [23] A.S. Saada, *Elasticity: Theory and Applications*, Pergamon Press, New York, 1974.
- [24] C. Pryor, *Phys. Rev. B* 57 (1998) 7190.
- [25] P. Sutter, M.G. Lagally, *Phys. Rev. Lett.* 81 (1998) 3471.
- [26] J. Demarest, Ph.D. Dissertation, University of Virginia, 2001, p. 172.
- [27] K. Muraki, S. Kukatsu, Y. Shirali, R. Ito, *Appl. Phys. Lett.* 61 (1992) 557.
- [28] C. Lanczos, *J. Res. Nat. Bur. Stand.* 45 (1950) 255.
- [29] J.K. Cullum, R.A. Willoughby, *Lanczos Algorithms for Large Symmetric Eigenvalue Computations*, Birkhauser, Boston, 1985.
- [30] C.G. Van der Walle, *Phys. Rev. B* 39 (1989) 1871.
- [31] G. Cipriani, M. Rosa-Clot, S. Taddei, *Phys. Rev. B* 61 (2000) 7536.
- [32] A.J. Williamson, A. Zunger, *Phys. Rev. B* 59 (1999) 15819.
- [33] O. Stier, M. Grundmann, D. Bimberg, *Phys. Rev. B* 59 (1999) 5688.
- [34] F.H. Pollak, *Semicond. Semimet.* 32 (1990) 17.
- [35] M.G. Burt, *J. Phys.: Condens. Matter* 4 (1992) 6651.
- [36] K.H. Schmidt, G. Medeiros-Ribeiro, M. Oestreich, G.H. Döhler, P.M. Petroff, *Phys. Rev. B* 54 (1996) 11346.
- [37] D. Pal, V.G. Stoleru, E. Towe, *Jpn. J. Appl. Phys.* 41 (1) (2001) 482.
- [38] C. Pryor, *Phys. Rev. B* 60 (1999) 2869.
- [39] S.L. Chuang, *Physics of Optoelectronic Devices*, Wiley, New York, 1995.
- [40] K.H. Hellwege, in: Landolt-Börnstein (Ed.), *Numerical Data and Functional Relationships in Science and Technology*, New Series, Group III 17a, Springer, Berlin, 1982; Groups III–V 22a, Springer, Berlin, 1986.

Interband emission and normal-incidence intraband absorption in (In,Ga)As quantum-dot nanostructures

D. Pal*, D. Firsov¹, E. Towe²

Laboratory for Optics and Quantum Electronics, University of Virginia, Charlottesville, VA 22904-4743, USA

Received 2 April 2001; accepted 27 November 2001

Abstract

This paper reports on interband emission and intraband absorption processes in doped InGaAs/GaAs quantum-dot nanostructures as the measurement temperature is varied. An analysis of the data yields useful insight into the carrier redistribution mechanisms that occur as a result of dot-size variation. For the samples studied, the size distribution is bimodal; this is reflected in the results obtained from the interband emission, as well as in the intraband absorption data. The understanding gained from studies such as these is important in the design of quantum-dot optoelectronic devices intended for room-temperature operation. © 2002 Elsevier Science B.V. All rights reserved.

PACS: 73.20.Dx; 78.55.Cr; 78.66.Fd

Keywords: Quantum dots; Photoluminescence; Absorption; Photodetectors; InGaAs/GaAs

Zero-dimensional quantum-dot nanostructures have recently become of considerable interest because of their potential application in electronic and optoelectronic devices. Some of the important characteristics of the nanostructures include: atom-like density of states, large exciton binding energies, and tunability of the emission and absorption wavelengths. These unique characteristics have stimulated a number of efforts aimed at developing a new generation of light-emitters and detectors [1,2].

* Corresponding author. Fax: +1-434-924-8818.

E-mail addresses: dp4b@virginia.edu (D. Pal), towe@cmu.edu (E. Towe).

¹ On leave from the St. Petersburg State Technical University, St. Petersburg, 195251, Russia.

² Present address: Carnegie Mellon University, Department of Electrical and Computer Engineering, 5000 Forbes Avenue, Pittsburgh, PA 15213-3891, USA.

In general, the ideal electronic or optoelectronic device should operate at room temperature. To enable this, it is desirable to have a clear understanding of the effects of temperature on the electronic and optical properties of the material out of which the device is fabricated. There have been some reports on the optical properties of quantum-dot nanostructures; specifically, there have been reports on the temperature-dependence of interband emission from InAs/GaAs [3], (In,Ga)As/GaAs [4] and (Al,In)As/(Al,Ga)As [5] quantum-dot structures. The emission from these structures has been observed to decrease with increasing temperature. This is probably due to the ejection of carriers from the dots by thermal excitation into the lowest-lying states in the wetting layer or into similar states in the matrix material. When this occurs, the usual radiative recombination processes no longer take place within

the dot—leading to a decrease in emission. A second possible pathway is a non-radiative recombination process; yet another pathway for quenching is the thermal redistribution of carriers within dots of different sizes [6]. The temperature-dependent carrier redistribution within dots of different sizes is generally thought to be responsible for the unusual line width variation. Furthermore, it is connected with the rapid red-shift of the photoluminescence emission peak. This red-shift is more pronounced than the usual temperature-dependent band gap change. We want to point out that the thermal redistribution of carriers in doped quantum-dot structures—such as those used in quantum-dot infrared photodetectors—is not yet fully understood. The redistribution of carriers at high temperatures can modify the intraband absorption on which these detectors depend. This, in turn, can affect the performance of the devices at elevated temperatures.

Normal-incidence intraband absorption has been reported in n-type doped InGaAs/GaAs [7] and InAs/GaAs [8] quantum dots. Phillips et al. have reported intraband absorption in a five-period InAs/GaAs quantum-dot structure at 300 K [9]. Other researchers have reported normal-incidence intraband absorption processes in InAs/InAlAs quantum-dot structures at 77 K [10]. However, there has not been any reports on the effect of carrier redistribution on the absorption strength.

In this paper, we present and discuss temperature-dependent results for interband, emission, as well as normal-incidence intraband absorption in doped, five-period InGaAs/GaAs quantum-dot nanostructures. The dot-sizes in these structures fall roughly into two groups: one group has a large dot-size, while another has a small dot-size. We find that the relative populations of the states in the two dot groups follow Boltzmann statistics. Finally, we measure an intraband absorbance of about 7.0% in our quantum-dot structures at 77 K.

Our structures were grown on (0 0 1) GaAs substrates in a solid-source molecular-beam epitaxy system. A typical structure consists of five periods of InGaAs/GaAs quantum-dot superlattice layers. The nominal Indium composition based on growth parameters and in situ RHEED observations, was about 30%. However the X-ray analysis of the sample showed that the average Indium composition in the

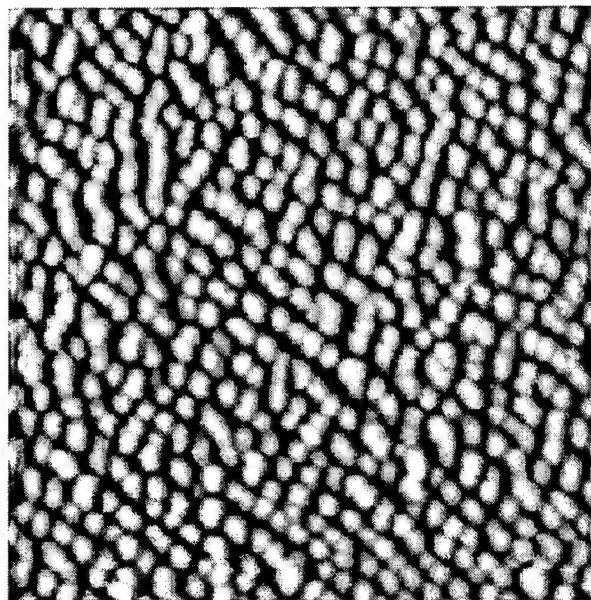


Fig. 1. AFM image ($1 \mu\text{m} \times 1 \mu\text{m}$) of InGaAs quantum dots.

dots is about 23%. The dots were delta-doped with Si to yield about two electrons per dot. The thickness of the GaAs barrier layer in the superlattice was about 50 nm. For atomic force microscope (AFM) studies, several uncapped samples were grown. These samples were grown under conditions identical to those used during the growth of the experimental structures.

Fig. 1 is a $1 \mu\text{m} \times 1 \mu\text{m}$ AFM micrograph of one of the uncapped InGaAs samples. The dot density is $\sim 6.34\text{--}6.8 \times 10^{10} \text{ cm}^{-2}$. Notice that the dots are closely packed and are not uniform in size. The dot heights vary from about 5–7.5 nm. We have plotted the statistical distribution of the lateral dot-size in the histogram shown in Fig. 2. This histogram shows a bimodal dot-size distribution. The average lateral extent of the majority of the dots is either ~ 28 or ~ 34 nm, as shown in the histogram. Note that there are apparently more small-size dots than large-size dots.

Photoluminescence measurements were carried out on the samples in the temperature range from 77 to 300 K using an Argon ion laser (488 nm) as the excitation source. The emitted radiation was detected with a liquid-nitrogen-cooled Ge photodetector. Normal-incidence intraband absorption measurements were performed with a BOMEM Fourier Transform Infrared spectrometer in the temperature range from 77 to 300 K.

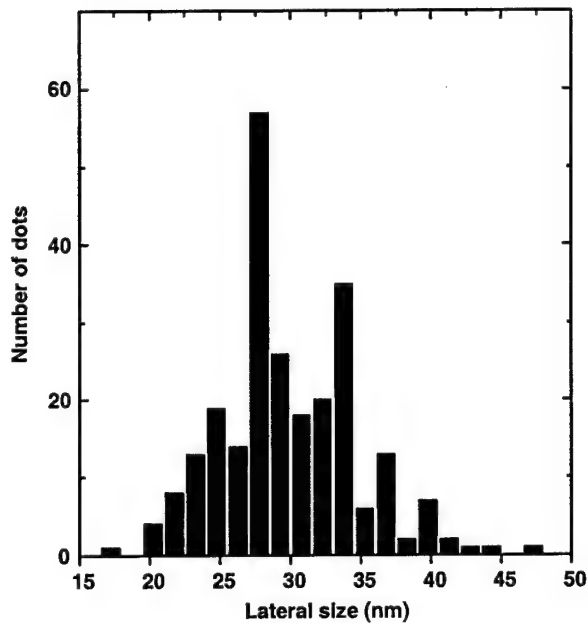


Fig. 2. Histogram of the lateral size distribution of InGaAs dots.

Fig. 3 shows typical photoluminescence emission spectra from one of our samples. At the low temperature of 77 K, the emission is characterized by a single, narrow peak at 1.19 eV, with a spectral spread of about 30.8 meV. As the temperature is increased, the spectrum broadens, and at about 300 K, in addition to the main peak at 1.12 eV, there is a distinct identifiable shoulder on the high-energy side of the spectrum. A deconvolution of this spectrum reveals the two spectra labeled (a) and (b), with peak energies at about 1.12 and 1.16 eV, respectively. The two peaks are separated by about 40 meV; this separation is smaller than the expected energy difference of 80–100 meV between the ground state and the first excited state in the conduction band of our typical dots. From intraband absorption measurements—which we will discuss later—the separation between the ground state and the first excited state in the conduction band is about 100 meV. This information suggests that the emission peak at 1.16 eV is probably not related to an interband transition from the first excited state in the conduction band of a certain group of dots to the relevant energy level in the valence band. A possible explanation is that the emission is associated with an interband transition from the ground

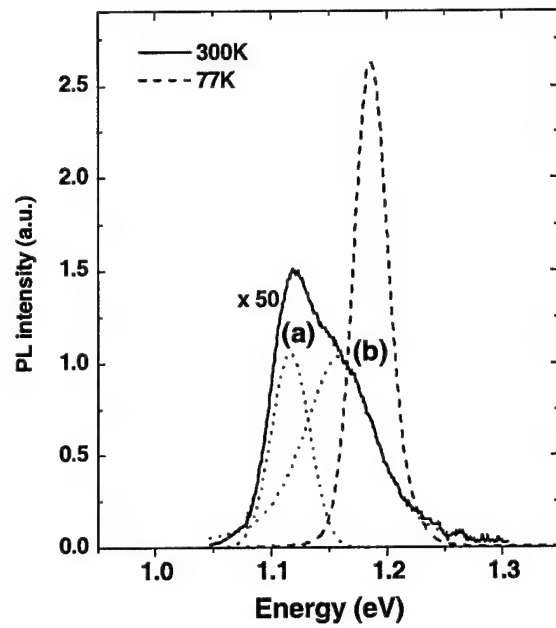


Fig. 3. The low (77 K) and room temperature (300 K) photoluminescence spectra of a five-period (In,Ga)As/GaAs quantum-dot nanostructure.

state of a different set of dots with a different average size.

The appearance of a suggestive shoulder (and hence a second peak) in the emission spectrum may be explained if we consider the bimodal dot-size distribution observed in the AFM images of the samples. The bimodal size distribution means that the dot population falls into two clusters, with the average size of one set of dots clearly identifiable as “small”, and another set with an average size that is “large”. During the optical excitation process, carriers, particularly holes in doped dots, tunnel out of the “small” dots into the “large” ones so that they can occupy the lowest possible energy states available in the ensemble. At 77 K, the luminescence from the dots that have the lowest possible ground states—that is: the large-size dots. This is the luminescence whose peak is observed at 1.19 eV. As the temperature is increased, thermal excitation begins to eject carriers out of the low energy states, leading to a redistribution such that dots of all sizes are occupied. For the bimodal size distribution observed in the atomic force microscope images of

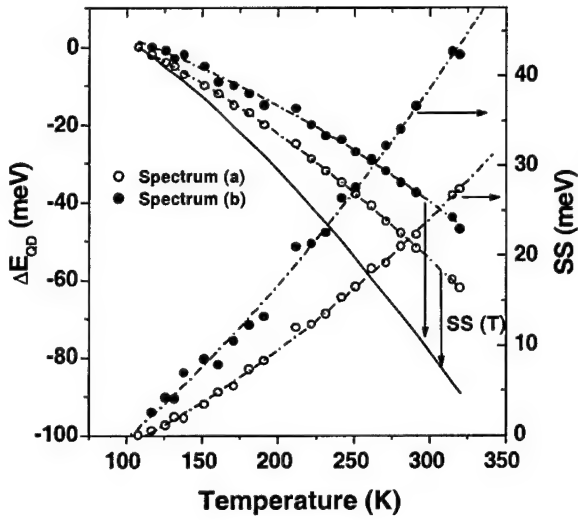


Fig. 4. The relative energy shift, ΔE_{QD} , as a function of temperature for bands (a) and (b), measured with reference to an emission peak at 107 K. The solid line shows the relative temperature-dependence of the band gap energy, ΔE_g , for InGaAs. The Stokes shift as a function of temperature is also shown (on the right-hand side abscissa).

our samples, the expected room-temperature luminescence is shown in Fig. 3; this spectrum can be resolved into the spectra (a) and (b). In this figure, spectrum (a) is attributed to transitions associated with the large-size dots; this is because the energy levels are located deeper at the bottom of the potential wells of the dots. The peak at 1.16 eV, in spectrum (b), is a result of transitions within the small dots.

The thermal redistribution of carriers can be followed systematically by observing a relative shift, ΔE_{QD} —from a fixed reference point—for each of the two emission peaks as the temperature is changed. We have chosen the single emission peak, $h\nu_{107 \text{ K}}$, observed at 107 K as the fixed reference point. The relative shift can then be given as $\Delta E_{\text{QD}} = h\nu(T) - h\nu(107 \text{ K})$, where $h\nu(T)$ is the temperature-dependent peak. Fig. 4 illustrates the relative temperature-dependent shift for the two spectra (a) and (b) of Fig. 3. For comparison, we show (with the solid line) the relative shift of the band gap energy of $\text{In}_{0.23}\text{Ga}_{0.77}\text{As}$ as calculated from $\Delta E_g = E_g(T) - E_g(107 \text{ K})$ according to Varshini's law [11].

In general, with no carrier redistribution processes involved, one would expect the photoluminescence

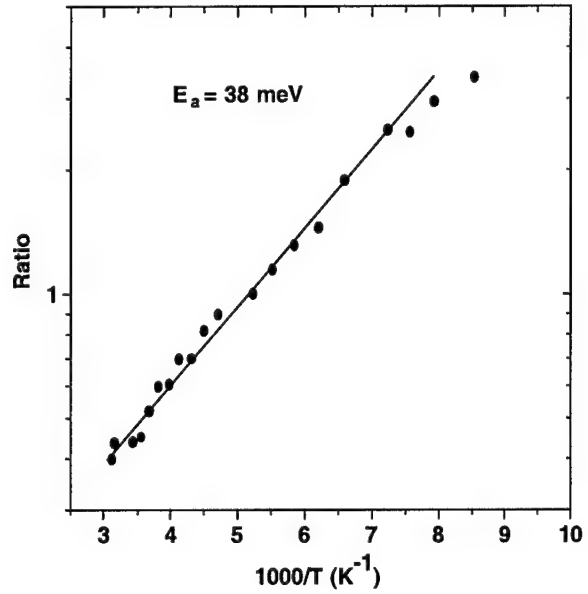


Fig. 5. The Arrhenius plot of the ratio of the integrated photoluminescence intensity of band (a) to band (b) as a function of temperature.

emission peak related to quantum-dot emission to follow a trend similar to that of the band gap with increasing temperature. This, however, is not the case. The relative rate of shift, $\partial\Delta E_{\text{QD}}/\partial T$, is small. If it were larger, it would indicate carrier redistribution from high to low energy states. This has been observed by Polimeni et al. in InAs quantum dots [12]. In our case, since the dots are very tightly packed, most of the carriers initially occupy the lowest energy states due to tunneling processes.

The energy difference, $\Delta E_{\text{QD}} - \Delta E_g$, is often defined as the Stokes shift (SS) between the luminescence and absorption lines. From Fig. 4, we see that the Stokes shift for spectrum (b) is larger than that for spectrum (a). This suggests that the dot-size distribution corresponding to emission band (b) is larger than that for band (a).

Another way to gain further insight into the carrier redistribution processes at high temperatures is to plot the ratio of the integrated photoluminescence intensity of spectrum (a) to spectrum (b) as a function of temperature. This ratio is shown in Fig. 5. The slope of the line in this figure yields an activation energy of about 38 meV. The energy difference (of 40 meV) between

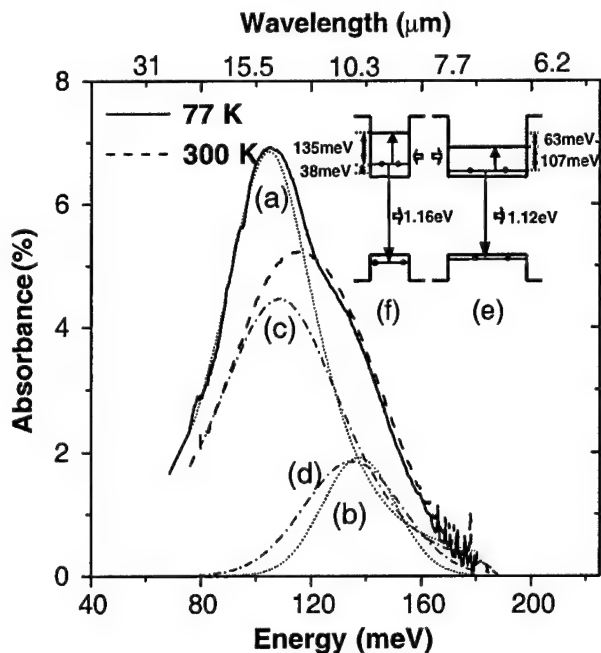


Fig. 6. Normal-incidence intraband absorbance spectra obtained at 77 and 300 K. Spectra (a) and (b) were obtained by deconvolution of the low-temperature (77 K) spectrum; spectra (c) and (d) were obtained as a result of deconvolving the room-temperature absorbance spectrum. A simple energy band diagram for the small- and large-size dots is in inset (f) for the small dots, and in inset (e) for the large dots.

the peak of spectrum (a) and spectrum (b) in Fig. 4 is quite close to the activation energy; this lends further support to the notion that carriers transfer from large-to-small-size dots. Similar results have been observed in undoped quantum-dot structures where the transfer of carriers, however, was from a dot layer to the wetting layer [13].

We now turn to the discussion of intraband absorption in our quantum-dot nanostructures. The absorption spectra, normalized to a background spectrum of a polished semi-insulating GaAs substrate without quantum dots on it, are shown in Fig. 6. The highest absorbance of 7% was recorded for a sample at 77 K; this is shown in spectrum (a). Our absorption measurements were performed at normal-incidence on a sample containing only five planes of quantum dot layers. The absorbance per quantum dot layer is therefore 1.4%. To our knowledge, this represents the highest absorbance ever reported for these structures.

We must, however, comment that very little data has been reported in the literature on absorbance. The few results that exist include data reported by Weber et al. [10]. This group reported low-temperature (77 K) absorbance data for InAs/InAlAs quantum-dot structures. Their absorbance per dot layer was 0.78%. In a paper by Phillips et al. [9], a room-temperature absorbance of about 0.48% per InAs/GaAs quantum-dot layer was reported. This value is lower than our room-temperature absorbance of 1.02% per layer of InGaAs dots.

The low- and room-temperature spectra in Fig. 6 show that the infrared absorption occurs at two energies—consistent with the photoluminescence results discussed earlier. A deconvolution of the low-temperature absorption spectrum reveals two resonances: one at 105 meV, as shown in curve (a), and another at 137 meV, shown in spectrum (b). The room-temperature spectrum can also be resolved into two spectra with peak energies at 107 and 135 meV. The corresponding integrated absorbance for spectrum (a) and spectrum (c) decreases from 3.2×10^{-3} to 2.4×10^{-3} as the temperature is raised from 77 to 300 K. On the other hand, the integrated absorbance increases from 6.3×10^{-4} for spectrum (b) to 8.2×10^{-4} for spectrum (d) as the temperature is raised from 77 to 300 K.

It is unlikely that the absorption spectra in Fig. 6 are a result of transitions from the ground state to the first- and second-excited states of the same set of dots. This is so because the integrated absorbance of the relevant sets of spectra does not decrease due to thermal escape of carriers from the dots. The integrated absorbance decreases only for the peak at ~ 105 meV while for the peak at ~ 135 meV, it increases with temperature.

The observed spectra are more likely to be from intraband transitions in large- and small-size dots. On the basis of our photoluminescence data and the intraband absorption results, one can derive a simple picture of the energy band structure (neglecting Coulomb charging effects) for the two sets of dots under discussion. Such a band structure is shown in the inset of Fig. 6. Here, we assume that the energy difference between the ground states in the valence band of the large- and small-size dots is approximately 2 meV. In the conduction band, the energy levels are as shown.

We have performed some theoretical calculations to determine the energy levels in the dots using an

eight-band $\mathbf{k} \cdot \mathbf{p}$ model with the strain effects included via deformation potential theory. The analytical approach developed by our group for the determination of strain fields and the associated energy structure has been presented elsewhere [14]. The energy level calculations assume that the large dots have a lateral extent of about 19.7 nm and a height of 3.0 nm; the small dots have a height of 3.0 nm and a lateral extent of ~ 16.8 nm. The geometry of the dots is truncated pyramidal. The calculated energy levels agree quite well with the experimental results. The lateral size and height of the dots used in the calculations are not the same as those obtained from the AFM studies. This is because: (i) dot-sizes cannot be accurately determined from AFM studies due to finite size and shape of the scanning probe, and (ii) the lateral size and height used in the calculations are for buried dots. During the growth of a GaAs over-layer, its morphology is affected by the interaction of the inhomogeneous strain in the neighborhood of the dots, as well as in the wetting layer. This interaction affects the apex of the dots. Thus, there is a thermodynamically favored tendency for the adatoms at the apex to migrate to the side of the dots [15]. One consequence of this migration is a reduction in the height of the buried dot and formation of a flat (0 0 1) surface.

As stated earlier, our nanostructure samples were doped to yield about 2 electrons per dot. Because of tunneling processes, the ground states of the large-size dots are the ones filled by most of the available electrons. The ground states of the small-size dots, on the other hand, may be partially filled or not filled at all. Thus, the intraband absorbance of the small-size dots is likely to be less than that of the large-size dots at lower temperatures. As the temperature is raised, a redistribution of the carriers takes place. Under equilibrium conditions, carrier transfer from large- to small-size dots is the most favored process. As a consequence, the number of electrons in the large-size dots decreases with increasing temperature. This, in turn, reduces the integrated absorbance as observed in our experiments. Since there are now more electrons in the small-size dots (as temperature is increased), the integrated absorbance increases; again, in agreement with our experimental observations.

The spectral widths of the absorption bands shown in Fig. 6 are fairly broad. In general, the spectral

spreads of interband and intraband transitions are a result of homogeneous and inhomogeneous broadening processes. Homogeneous broadening, which is due to different types of scattering mechanisms, usually gives rise to a Lorentzian line shape. Inhomogeneous broadening, on the other hand, is a consequence of the size distribution in the dot population. This type of broadening gives rise to a Gaussian line shape. The emission and absorption spectra observed here could not be fitted to a single type of line shape, Lorentzian or Gaussian. Only a mixture of both line shapes gives spectra that agree with the experimental and deconvoluted analytical data. This fact supports the notion that there is indeed a size distribution in the dot population.

In summary, we have studied the effects of carrier redistribution with temperature in dots of different sizes by observing the manifestations of interband and intraband transitions via luminescence and absorption experiments. These experiments are important in the understanding of the behavior of new or improved optoelectronic devices fabricated from quantum-dot nanostructures intended for room-temperature operation.

The authors acknowledge the generous support of the US Army Research Office, Research Triangle Park, North Carolina, and that of the US Army Research Laboratory, Adelphi, Maryland. We also acknowledge contributions to this paper by G. Stoleru and D. Pan.

References

- [1] F. Heinrichsdorff, Ch. Ribbat, M. Grundmann, D. Bimberg, *Appl. Phys. Lett.* 76 (2000) 556.
- [2] D. Pan, E. Towe, S. Kennerly, *Electron Lett.* 34 (1998) 1019.
- [3] D.I. Lubyshev, P.P. González-Borrero, E. Marega Jr., E. Petiprez, N. la Scala Jr., P. Basmaji, *Appl. Phys. Lett.* 68 (1996) 205.
- [4] R.P. Mirin, J.P. Ibbetson, K. Nishi, A.C. Gosard, J.E. Bowers, *Appl. Phys. Lett.* 67 (1995) 3795.
- [5] S. Fafard, S. Raymond, G. Wang, R. Leon, D. Leonard, S. Charbonneau, J.L. Merz, P.M. Petroff, J.E. Bowers, *Surf. Sci.* 361 (1996) 778.
- [6] Y.T. Dai, J.C. Fan, Y.F. Chen, R.M. Lin, S.C. Lee, H.H. Lin, *J. Appl. Phys.* 82 (1997) 4489.
- [7] D. Pan, E. Towe, S. Kennerly, *Appl. Phys. Lett.* 73 (1998) 1937.
- [8] L. Chu, A. Zrenner, G. Böhm, G. Abstreiter, *Appl. Phys. Lett.* 75 (1999) 3599.

- [9] J. Phillips, P. Bhattacharya, S.W. Kennerly, D.W. Beckman, M. Datta, *IEEE J. Quantum Electron.* 35 (1999) 936.
- [10] A. Weber, O. Gauthier-Lafaye, F.H. Julien, J. Brault, M. Gendry, Y. Désie, T. Benyatton, *Appl. Phys. Lett.* 74 (1999) 413.
- [11] Y.P. Varshni, *Physica (Netherlands)* 34 (1967) 149.
- [12] A. Polimeni, A. Patanè, M. Henini, L. Eaves, P.C. Main, *Phys. Rev. B* 59 (1999) 5064.
- [13] A. Patanè, A. Polimeni, P.C. Main, M. Henini, L. Eaves, *Appl. Phys. Lett.* 75 (1999) 814.
- [14] V.G. Stoleru, D. Pal, E. Towe, *Material Research Society Symposium Proceedings*, Vol. 642, Materials Research Society, Warrendale, PA, 2001, p. J1.7.1.
- [15] N.N. Ledentsov, V.A. Shchukin, M. Grundmann, N. Kirstaedter, J. Böhmer, O. Schmidt, D. Bimberg, V.M. Ustinov, A.Yu. Egorov, A.E. Zhukov, P.S. Kop'ev, S.V. Zaitsev, N.Yu. Gordeev, Zh.I. Alferov, A.I. Borovkov, A.O. Kosogov, S.S. Ruvimov, P. Werner, U. Gösele, J. Heydenreich, *Phys. Rev. B* 54 (1996) 8743.

Enhanced 1.3- μ m-emission from InAs quantum dots embedded in symmetric (In,Ga)As quantum-well structures

L. Chen, V.G. Stoleru, D. Pan¹, E. Towe*

Laboratory for Photonics, Department of Electrical and Computer Engineering, Carnegie Mellon University, 5000 Forbes Avenue, Pittsburgh, PA 15213, USA

Received 18 November 2001; accepted 21 April 2002

Communicated by D.W. Shaw

Abstract

We have optically characterized the emission of a layer of InAs quantum dots embedded at the center of symmetric (In,Ga)As quantum-well structures. By grading the profile of the indium composition in the quantum-well regions in a certain way, it is found that the room-temperature emission of the dots can be enhanced by almost an order of magnitude compared to dots bounded by conventional (In,Ga)As quantum wells. The largest enhancement is obtained for structures where the grading is achieved by using a GaAs/InAs superlattice structure to form a quasi-linear distribution of the indium. The dots inside the graded quantum-well structures are engineered to emit at the important telecommunication wavelength of 1.3 μ m. © 2002 Published by Elsevier Science B.V.

PACS: 73.61.Ey; 73.63.Kv; 68.35.Bs; 78.66.Fd

Keywords: A1. Low dimensional structures; A1. Optical microscopy; A3. Molecular beam epitaxy; B1. Nanomaterials; B3. Laser diodes

The first GaAs-based quantum-dot laser was reported in 1994 [1]. Since then, remarkable progress has been made in the development of this device. Edge-emitting lasers operating from 1.0 to 1.3 μ m with very low-threshold currents have been reported [2,3,9]; in addition, vertical-cavity surface-emitting lasers have been successfully demonstrated [4]. One of the advantages of utilizing GaAs-based quantum dots for fabricating

infrared lasers (at 1.3 μ m) is that the mature manufacturing and processing technology for this materials system can be brought to bear in the production of these lasers for data and telecommunication applications.

There are currently several approaches utilized in the (molecular beam epitaxial) synthesis of (In,Ga)As/GaAs quantum dots that emit at 1.3 μ m. These include (i) the alternate supply of the group-III indium and the group-V arsenic source materials to form the InAs dots [5], (ii) slow growth (<0.01 ML/s) of the InAs dots at high substrate temperatures [6], (iii) burying the InAs dots with an (In,Ga)As (rather than a GaAs)

*Corresponding author.

E-mail addresses: lc2k@virginia.edu (L. Chen), towe@cmu.edu (E. Towe).

¹Also at: 9 Baron Lane, Burlington, MA 01803, USA.

overlayer to reduce the strain [7], and (iv) embedding the InAs dots inside an (In,Ga)As quantum-well structure [8]. The basic physical effect in the first two approaches is the formation of large-size dots, which result in a small effective quantum-dot bandgap whose consequence is long-wavelength emission when the dots are optically or electrically pumped. In approach (iii) and (iv), the (In,Ga)As layers play the role of reducing the lattice-mismatch-induced strain around the InAs dots.

Most quantum-dot lasers operating at $1.3\text{ }\mu\text{m}$ appear to have two major unresolved problems: a low density of dots and a weak carrier confinement to the active region. Both of these problems imply low optical gain. In fact, the low gain is believed to prohibit the lasers from operating at the ground state without high-reflectivity coatings [3,10]. One approach to achieving tight carrier confinement is to use growth method (iv), which embeds the dots in an (In,Ga)As quantum-well layer. In addition to serving as a strain reducing (and hence a wavelength tuning) layer, the (InGa)As quantum well also serves to confine carriers within the vicinity of the quantum-dot layer, thus promoting capture within the dots [9].

In this paper, we show that additional deliberate strain, and hence band structure engineering of the InAs/(In,Ga)As quantum-dot and (In,Ga)As/GaAs quantum-well layers can result in a controllable tuning of the emission wavelength; furthermore, these structures promote an increase in the luminescence efficiency.

The samples in our study were grown in a solid-source molecular-beam epitaxy system on semi-insulating (001) GaAs substrates. The basic structure consists of InAs quantum dots symmetrically sandwiched between two (In,Ga)As layers; this structure, in turn, is inserted at the center of a 180-nm-GaAs layer on top of a 250-nm-GaAs buffer layer on a (001) GaAs substrate. The 250-nm-GaAs buffer layer was grown at a substrate temperature of 580°C . The temperature was then gradually lowered to 490°C [17] during the growth of the 90-nm-GaAs layer which precedes the growth of the bottom InGaAs layer on top of which the InAs dots are grown. The rest of the structure was grown at 490°C . Three samples,

different in the essential details of their band structures, were grown. A schematic of the generic structure is shown in Fig. 1 for all three samples. Sample A consists of 2.5 ML of InAs quantum dots sandwiched at the center of an 8-nm-In_{0.15}Ga_{0.85}As layer. Sample B consists of 2.5 ML of InAs quantum dots sandwiched at the center of an 8-nm-In_xGa_{1-x}As layer; the bottom half of the In_xGa_{1-x}As layer is graded from $x = 0.03$ to 0.3; the top half is graded from $x = 0.3$ to 0.03. The change of indium composition, x , in the graded In_xGa_{1-x}As quantum-well region is achieved by gradually increasing or decreasing the indium cell temperature as a function of time. The structure of sample C is similar to that of sample B except that InAs/GaAs superlattice layers are used to form the quasi-linear indium distribution along the growth direction (see Fig. 1). The InAs/GaAs superlattice we use in sample C consists of nine periods of InAs/GaAs, where the thickness of the GaAs layer in each period is 4 Å; the thickness of the InAs layer in each period is determined by the temporal duration of each period, which is increased in an ordinal sequence from 1 to 9 s, or decreased from 9 to 1 s. The growth rate of the InAs dots was 0.05 ML/s, and the As₄ over-pressure was maintained at 4.0×10^{-6} Torr during the growth of all the samples. The substrate holder was continuously rotated to improve the uniformity. Another set of samples, grown under identical conditions, but without the layers that cover the dots was

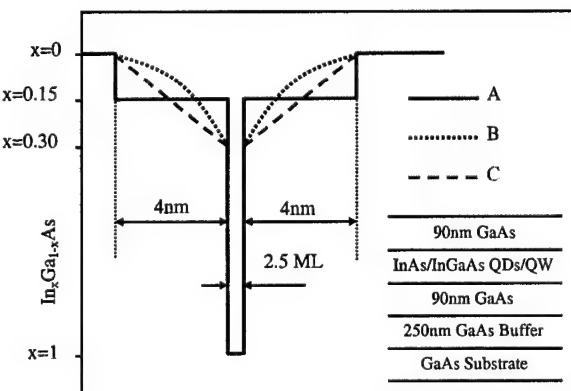


Fig. 1. Schematic of the conduction band structure of quantum-dot samples embedded at the center of quantum-well structures. The inset shows the physical layer structure.

grown for atomic force microscope (AFM) surface studies. We want to comment that during the epitaxy of samples B and C, the reflection high-energy electron diffraction (RHEED) pattern was observed to gradually dim during the growth of the graded $\text{In}_x\text{Ga}_{1-x}\text{As}$ layer adjacent to the GaAs buffer. For sample A, however, the RHEED intensity was abruptly dimmed after a few seconds. This sample consisted of an $\text{In}_{0.15}\text{Ga}_{0.85}\text{As}$ layer grown directly adjacent to the GaAs buffer layer without any intermediate grading.

Our samples were characterized by photoluminescence spectroscopy at both room temperature (295 K) and low temperature (78 K). All the samples were mounted on a flat copper plate whose temperature could be controlled. An Argon ion laser, emitting at 488 nm, was used as an excitation source; the emitted radiation was detected with a cooled Ge detector.

The room-temperature photoluminescence spectra of samples A, B, and C are shown in Fig. 2. The emission from the ground-state transition for all three samples is at or beyond 1.3 μm , with sample C extending to 1.35 μm . The spectral linewidths, at half-maximum intensity, for the samples are $\Delta\nu_A = 48 \text{ meV}$, $\Delta\nu_B = 53 \text{ meV}$, and $\Delta\nu_C = 39 \text{ meV}$, respectively. These linewidths are fairly broad, indicating the effects of inhomogeneous broadening due to the variation of the dot-

sizes. The grading of the $\text{In}_x\text{Ga}_{1-x}\text{As}$ quantum-well confining layers does not have any apparent effect on the uniformity of the dots-sizes. What the grading does appear to do is to improve the efficiency of emission. From Fig. 2, it is evident that there is an enhancement of the photoluminescence emission intensity for samples B and C. All three samples were excited with the same flux, under the same testing conditions. The peak intensity for sample C, for example, is about 8.7 times higher than that for sample A. We have also performed X-ray diffraction measurements on the samples to evaluate the overall strain in the structures using the [004] reflection. The X-ray measurements were performed using a Phillips MRD system. The average strain in the structures, parallel to the growth direction, was determined as 1.12×10^{-2} for sample A, 1.02×10^{-2} for sample B, and 1.13×10^{-2} for sample C. The corresponding indium compositions were 15.7% for sample A, 14.3% for sample B, and 15.8% for sample C. The slightly lower indium composition for sample B is due to the non-linear relationship between the indium cell temperature and the flux arrival rate at the growth surface during the grading. Since in these samples, the only significant difference is the structure of the $\text{In}_x\text{Ga}_{1-x}\text{As}$ layer into which the quantum dots are embedded, it is reasonable to speculate that the enhancement in luminescence intensity is due to the nature of the grading. There may be two possible reasons that account for this enhancement. One is that, in a graded QW, the energy band may also be graded; this leads to the existence of a field which helps accelerate the carriers along the quantum-well gradient, and hence into the quantum dots. Because of the three-dimensional nature of quantum dots, the graded potential also exists in the lateral direction; this enhances the spatial carrier capture within the dots. The second reason for the enhancement of luminescence is the smoothing effect of the InAs/GaAs superlattice. The superlattice causes the transition of the lattice parameter from that of GaAs to the one InAs to be continuously smooth, thus reducing the formation of lattice-mismatch-induced defects. The defects, if present, would form loss channels in the electron–hole recombination process. Of the two grading techniques

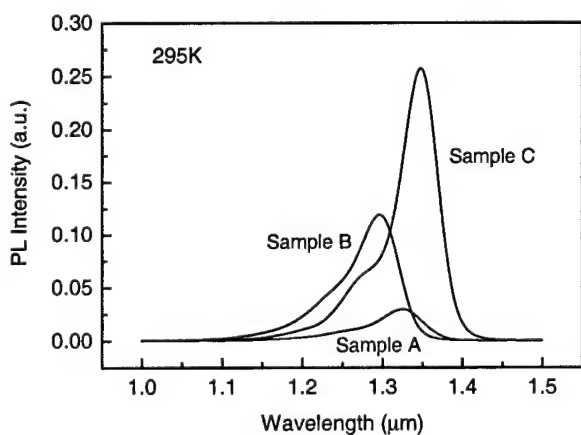


Fig. 2. Room-temperature photoluminescence spectra of the quantum-dot samples at an optical excitation level of $\sim 30 \text{ W/cm}^2$.

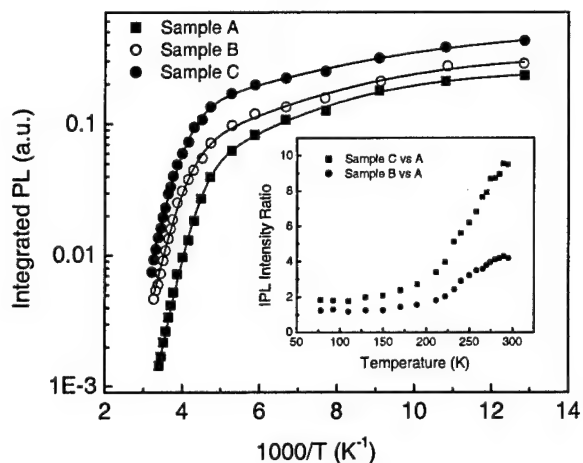


Fig. 3. The Arrhenius plots of the integrated luminescence intensity of samples A, B and C for the optical excitation level of $\sim 10 \text{ W/cm}^2$. The solid lines are fitted to Eq. (1) in the text. The inset shows the ratio of the integrated luminescence intensity of sample B to sample A, and of sample C to sample A as a function of temperature.

used, the quasi-linear grading method of sample C yields the better results.

We have further studied the temperature-dependent integrated luminescence intensity of the samples. The Arrhenius plots for the samples are shown in Fig. 3. The variation of the integrated intensity data with temperature can be described by the generic empirical relationship [11]

$$I(T) =$$

$$\frac{I_0}{1 + C_1 \exp(-E_1/kT) + C_2 \exp(-E_2/kT)}, \quad (1)$$

where E_1 and E_2 are the thermal activation energies for loss mechanisms active at certain temperature ranges, k is the Boltzmann constant, T is the temperature, and I_0 , C_1 and C_2 are (fitting) constants. In a physical model, these constants would take into account the recombination rates and the geometric dimensions of the dots. The fitting parameters and extracted activation energies are given in Table 1. In Fig. 3, the solid lines show the fit to the data using Eq. (1) given above; the filled circles, open circles, and squares represent experimental data. The extracted activation energies are $E_1 = 289 \text{ meV}$, and $E_2 = 41 \text{ meV}$ for sample A; $E_1 = 263 \text{ meV}$, and $E_2 = 33 \text{ meV}$ for sample B; and $E_1 = 255 \text{ meV}$ and $E_2 = 25 \text{ meV}$

Table 1

Sample	Fitting parameters		Activation energies (meV)		
	I_0	$C_1 \times 10^6$	C_2	E_1	
A	0.252	14.8	32.7	289	41
B	0.334	1.34	18.6	263	33
C	0.532	0.706	9.31	255	25

for sample C. Note that the luminescence intensity has a quenching threshold temperature; for both sample B and C this temperature is $\sim 190 \text{ K}$, and it is $\sim 170 \text{ K}$ for sample A. The loss channel that dominates at these high temperatures is probably associated with the activation energy E_1 . A calculation (which we will discuss later) shows that the energy difference between the ground state in the conduction band of a dot and the band-edge of the surrounding (In,Ga)As quantum well at 300 K is about 317 meV for structure A and 267 meV for sample C. These energy differences are quite close to the measured activation energies E_1 for samples A and C. At the quenching threshold temperatures, the thermal escape of carriers from the dots begins to play an important role in carrier recombination dynamics. It is then conceivable that the carriers have sufficient energy to overcome these barriers. An interesting aspect of the comparison between the recombination dynamics of our samples is that the photoluminescence enhancements of samples C and B are more dramatic at the higher temperatures (see the inset in Fig. 3). Our results here are similar to those of Ru et al. who used hydrogen passivation (in order to reduce the defect concentrations in their samples) to enhance the photoluminescence emission [12]. In our case, grading of the QW (and the use of the superlattice in sample C) may reduce the tendency for lattice-mismatch-induced formation of defects at the QW/QD interface region, thus reducing non-radiative defect-related losses in the structures.

We have examined the possible effects of the grading on the dot density and uniformity. Three structures similar to samples A, B and C were grown for AFM observations. Fig. 4 shows the

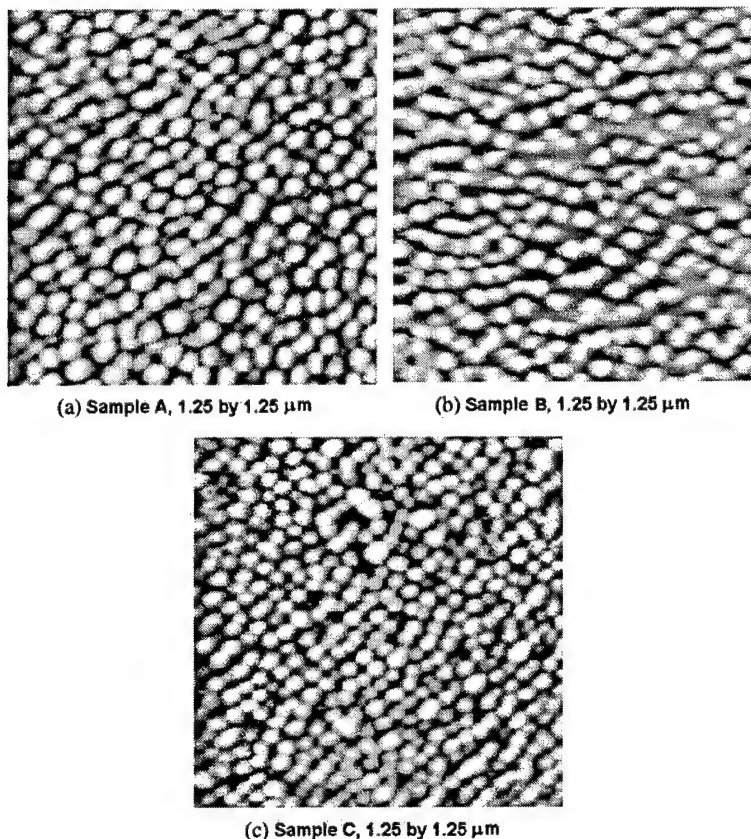


Fig. 4. AFM photo-micrographs of the morphology of samples A, B, and C.

AFM micrographs of the three samples. The areal dot densities of these samples are $2.5 \times 10^{10} \text{ cm}^{-2}$ for sample A, $1.8 \times 10^{10} \text{ cm}^{-2}$ for sample B, and $2.8 \times 10^{10} \text{ cm}^{-2}$ for sample C. The true size of the dots cannot be determined from the AFM measurements; reasonable estimates, however, can be obtained from cross-sectional TEM studies.

To show the basic quantum-confined features of the band structure of the samples, we have studied the intensity-dependent photoluminescence emission at both room and LN_2 temperatures. In Fig. 5, we show the LN_2 (78 K) photoluminescence emission for the three samples at high pump levels. There are clearly four transition energy peaks for each sample. We have carried out some analytical calculations to determine the locations of the interband transition energies for samples A and C. Because of the non-linear composition of the indium in the QW region of sample B, we have, for simplicity, omitted it in our calculations. These

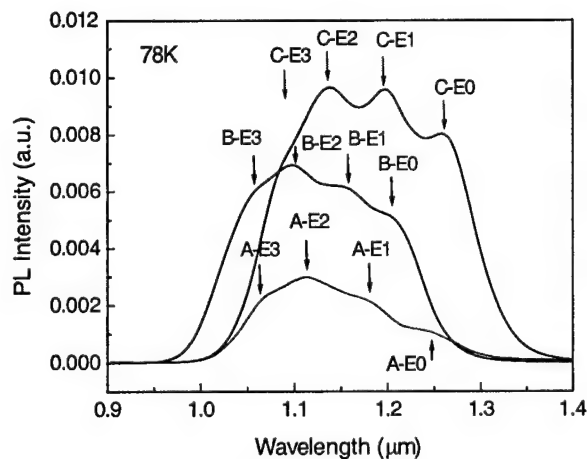


Fig. 5. The low-temperature (78 K) photoluminescence spectra of samples A, B, and C under high optical excitation.

calculations require information on the strain distribution inside and around the dots. The strain generally depends on the shape and size of the

Table 2

Structure	Data source	Transition energy (eV)				
		Low temperature (77 K)				RT (300 K)
		E_0	E_1	E_2	E_3	
A	Experimental	1.019	1.056	1.102	1.154	0.934
	Calculated	1.0162	1.0572	1.0951	1.1500	0.9405
C	Experimental	0.987	1.036	1.083	1.139	0.919
	Calculated	0.9830	1.0379	1.0809	1.1315	0.9138

dots, which are difficult to determine accurately in most experimental situations. For our dots, we estimate their lateral extent (base) to be around 15 nm; the base-to-height ratio for sample A is about 7; and it is 5 for sample C. These estimates are based on our earlier work on buried InAs/GaAs and InGaAs/GaAs quantum-dot work [13], and on TEM and SEM observations. The estimate on height is further corroborated with in-situ RHEED observations where the thickness of an over-layer needed to completely bury an array of dots (so that the layer-by-layer growth mode is re-established) can give a rough measure of the dot height. For the calculations, we have further assumed that the dots are truncated pyramids.

The electronic spectra here are calculated in the envelope function approximation using an eight-band, strain-dependent Hamiltonian based on the $\mathbf{k} \cdot \mathbf{p}$ method [14]. The details of the method we use in the calculations have been published elsewhere [15,16]. The calculated transition energies for our samples A and C are shown in Table 2. We have also shown the experimentally determined values from the photoluminescence data obtained from multi-peak Gaussian fitting. The experimental and the calculated transition energies are in reasonably good agreement.

In summary, we have shown that the photoluminescence efficiency of (In,Ga)As/GaAs quantum dots can be enhanced by embedding them in a graded (In,Ga)As quantum-well structures. We believe this approach is simpler and more practical than the use of in situ hydrogen passivation for defect annealing. Furthermore, our proposed approach has the virtue of promoting carrier

capture in potential laser structures in addition to allowing emission at the desirable telecommunications wavelength of 1.3 μm . The band grading we describe here is reminiscent of the graded index, separate confinement heterostructures (GRINSCH) of early generation active regions of quantum-well lasers.

This work is supported under Grant Number DAAD19-00-1-0442 of the US Army Research Office, Research Triangle Park, North Carolina, and by the US Army Research Laboratory, Adelphi, Maryland. The experimental work reported here was conducted while the authors were affiliated with the University of Virginia, Charlottesville, Virginia.

References

- [1] N. Kirkstaedter, N. Ledentsov, M. Grundmann, D. Bimberg, V. Ustinov, S. Ruvimov, M. Maximov, P. Kop'ev, *Zh. Alferov*, Electron. Lett. 30 (1994) 1416.
- [2] G. Park, O.B. Shchekin, D.L. Huffaker, D.G. Deppe, *IEEE Photon. Tech. Lett.* 12 (2000) 230.
- [3] D.L. Huffaker, G. Park, Z. Zou, O.B. Shchekin, D.G. Deppe, *Appl. Phys. Lett.* 73 (1998) 2564.
- [4] J.A. Lott, N. Ledentsov, V. Ustinov, N.A. Maleev, A.E. Zhukov, A.R. Kovsh, M.V. Maximov, B.V. Volovik, *Zh.I. Alferov*, D. Bimberg, Electron. Lett. 36 (2000) 1384.
- [5] D.L. Huffaker, D.G. Deppe, *Appl. Phys. Lett.* 73 (1998) 520.
- [6] R. Murray, D. Childs, S. Malik, P. Sivers, C. Roberts, J.M. Hartmann, P. Stavrinou, *Jpn. J. Appl. Phys.* 38 (1999) 528.
- [7] K. Nishi, H. Saito, S. Sugou, *Appl. Phys. Lett.* 74 (1999) 1111.

- [8] A. Stintz, G.T. Liu, H. Li, L.F. Lester, K.J. Malloy, IEEE Photon. Tech. Lett. 12 (2000) 591.
- [9] G.T. Liu, A. Stintz, H. Li, T.C. Newell, A.L. Gray, P.M. Varangis, K.J. Malloy, L.F. Lester, IEEE J. Quantum Electron. 36 (2000) 1273.
- [10] N. Hatori, M. Sugawara, K. Mukai, Y. Nakata, H. Ishikawa, Appl. Phys. Lett. 77 (2000) 773.
- [11] Y. Wu, K. Arai, T. Yao, Phys. Rev. B 53 (1996) 10485.
- [12] E.C. Le Ru, P.D. Sivers, R. Murray, Appl. Phys. Lett. 77 (2000) 2446.
- [13] V.G. Stoleru, D. Pal, E. Towe, Mater. Res. Soc. Proc. 642 (2000) J171–6.
- [14] T.B. Bahder, Phys. Rev. B 41 (1992) 11992.
- [15] D. Pal, V.G. Stoleru, E. Towe, D. Firsov, Jpn. J. Appl. Phys. Part 1 41 (2A) (2002) 482.
- [16] V.G. Stoleru, D. Pal, E. Towe, Physica E, 2002, accepted for publication.
- [17] A. Stintz, G.T. Liu, A.L. Gray, R. Spillers, S.M. Delgado, K.J. Malloy, J. Vac. Sci. Technol. B 18 (3) (2000) 1496.

Quantum Dot-Size Variation and Its Impact on Emission and Absorption Characteristics: An Experimental and Theoretical Modeling Investigation

D. PAL*, V. G. STOLERU, E. TOWE[†] and D. FIRSOV¹

*Laboratory for Optics and Quantum Electronics, Department of Electrical and Computer Engineering,
University of Virginia Charlottesville, VA 22904-4743, USA*

¹*St. Petersburg State Technical University, St. Petersburg, 195251, Russia*

(Received July 2, 2001; revised manuscript received November 8, 2001; accepted for publication November 12, 2001)

This paper presents a study of electronic carrier redistribution in doped (In, Ga)As/GaAs quantum dots due to size variation. The dots in our samples fall roughly into “large” and “small” size clusters. At low temperatures, the carriers predominantly occupy the large-size dots. As the sample temperature is raised, thermal energy redistributes the carriers so that some begin to occupy energy states in the small-size dots. At room-temperature, the photoluminescence emission spectrum exhibits two distinct peaks due to transitions from the large- and small-size dots. This carrier redistribution can also be followed by observing the integrated absorbance as a function of temperature. The transition energy levels extracted from photoluminescence data compare favorably with theoretically calculated values for dots with truncated pyramidal shapes. [DOI: 10.1143/JJAP.41.482]

KEYWORDS: quantum dots, intraband absorption, photoluminescence, (In, Ga)As/GaAs, nanostructures, strain, carrier redistribution, quantum dot-size distribution

1. Introduction

The study of semiconductor quantum-dot nanostructures has attracted considerable interest in the last few years. This is because of the potential application of the dots in electronic and optoelectronic devices. These nanostructures confine carriers in all three dimensions. As a consequence of this, several important characteristics emerge: these include atom-like density of states, large exciton binding energies, and enhanced oscillator strengths. Some of these characteristics have enabled the demonstration of novel light-emitting sources,¹⁾ single-electron memory elements,²⁾ and infrared photodetectors.³⁾ Of the devices demonstrated so far, perhaps the most advanced is the interband laser;^{1,4)} it has operated at both low-temperatures and room-temperature. The interband quantum-dot laser has also been shown to exhibit a high characteristic temperature, T_0 —which is a measure of the sensitivity of the threshold current to temperature variations.

The intraband absorption properties of the dots have been used to design and fabricate infrared photodetectors. These devices, however, have only operated at cryogenic temperatures so far.^{5,6)} Further development for high-temperature operation will require an understanding of the effects of temperature on the intraband absorption characteristics. In fact, a better understanding of the effects of temperature on both the interband and intraband emission and absorption characteristics of the dots would be helpful in the design of future room-temperature devices. Several workers have reported the effects of temperature on interband emission from InAs/GaAs, (In, Ga)As/GaAs, and (Al, In)As/(Al, -Ga)As quantum-dot structures.^{7–9)} It has been found that in some cases, the emission intensity from the nanostructures is quenched as the temperature is raised. When dots of different sizes exist in an ensemble, the variation in temperature has been linked to a thermal redistribution of carriers within the ensemble. These observations were made on undoped quantum dots; no studies on doped nanostruc-

tures have yet been reported. The emission and absorption behavior of doped quantum dots, as the temperature is changed, is important because it has a direct bearing on the operating characteristics of many optoelectronic devices.

While most of the work in the literature on quantum dots has focused on dot emission characteristics, there is now a growing interest in absorption: the inverse of emission. Absorption provides a unique signature for the energy structure in the quantum dots. Normal-incidence intraband absorption, for example, can provide information on intersublevel energy separations. Several groups have reported low-temperature photoconduction spectroscopy measurements in n-type, doped (In, Ga)As/GaAs³⁾ and InAs/GaAs¹⁰⁾ dots. The work on InAs dots has been performed at both low- and room-temperatures.^{11,12)} Since most dot systems studied to date contain distinct size distributions, it would be interesting to know the effect of thermal carrier redistribution on the absorption strengths of the dot systems.

One of the most challenging aspects of quantum-dot work is the development of quantitative models that accurately describe the dots synthesized from III–V compound semiconductors. A number of elegant theoretical models exist;^{13,14)} the shapes of the dots and the parameters used in the theoretical calculations, however, often yield results that are difficult to match to experimental data. As a consequence, the models have not played a significant role in guiding experimentation. Several groups are therefore engaged in the development of models that best suit their experimental situation. In this work, we use a transmission electron microscope (TEM) to experimentally determine the shape of the dots. Our observations lead us to believe that the dots grown in our laboratory are predominantly truncated pyramids. We use the dimensions and shape extracted from the TEM images in calculations of the energy levels in the dots. In these calculations, one must take into account the effects of strain—which, in the first place, is responsible for the formation of the dots. Two of the most common methods used in the quantitative analysis of strain involve spatial discretization of the region within which the strain is known

*E-mail: dp4b@virginia.edu

[†]E-mail: towe@emu.edu

to exist: the first method is the finite element technique¹⁴⁾ and the second is the finite difference method.¹⁵⁾ Both techniques require considerable computational resources. In this work we will use a simple analytical technique for calculating the strain distribution in and around the dot. The results of the strain calculations are a precursor to the energy structure analysis.

Our aim in this paper is to: (a) show the effects of temperature on the luminescence characteristics of Si-doped (In, Ga)As quantum dots and the associated Boltzmann redistribution of carriers in dot ensembles with size variations in them; (b) show that the doped dots exhibit strong, normal-incidence, intraband absorption; and (c) compare the experimentally determined energy levels in our quantum dots with values derived from calculations.

2. Experimental

The quantum-dot superlattices used in this study were grown by a solid-source molecular beam epitaxy system. A typical structure consists of five periods of (In, Ga)As/GaAs quantum dots grown on a (001) GaAs substrate. The nominal indium composition, based on growth parameters and *in-situ* RHEED observations, was about 30%. X-ray analysis of the samples, however, indicated that the average indium composition in the dots was about 23%. The dots were δ -doped with silicon to yield about two electrons per dot. The thickness of the GaAs barrier layer in the superlattice was about 50 nm. An uncapped sample was also grown using identical growth parameters for surface analysis of the dots by an atomic force microscope. The surface studies indicate that the density of the dots is about $6.3\text{--}6.8 \times 10^{10} \text{ cm}^{-2}$, and from high-resolution transmission electron microscopy, we were able to determine that the buried dots are about 3 nm high; the lateral extent of their bases ranged from about 16 to 20 nm.

2.1 Photoluminescence

Photoluminescence measurements were carried out using an argon-ion laser ($\lambda = 488 \text{ nm}$) as the excitation source. The temperature of the samples was varied from 77 to 300 K. The emitted radiation was detected with a cooled Ge detector. Figure 1 shows the luminescence spectra obtained as the temperature is varied from liquid-nitrogen (77 K) to room-temperature (300 K). Note the quenching of the peak intensity as the temperature is raised; also observe that as the temperature approaches 300 K, the spectrum broadens and there is a suggestion of a second peak hidden by the broad emission. This is clearly shown in the room-temperature spectrum of Fig. 2; at low-temperature (77 K), however, the emission is characterized by a single peak located at 1.19 eV, with a spectral spread of about 30.8 meV. Furthermore, no luminescence from the states in the wetting layer was observed due to photo-generated carriers in the wetting layer transfer into the adjacent dots. A deconvolution of the room-temperature spectrum indicates that it is, indeed, a composite of two spectra with peaks located at 1.12 and 1.16 eV. These spectra have been labeled (a) and (b) in Fig. 2. The energy difference between the peaks is about 40 meV; this is much smaller than the nominal separation (80–100 meV) between the ground state and the first excited state of the conduction band of our quantum

dots. From intraband absorption measurements (to be discussed later), the nominal separation should be about 100 meV. The appearance of the second peak—on the high energy side of the room-temperature spectrum—therefore cannot be attributed to an excited state transition. One can explain the appearance of the second peak by considering a bimodal size distribution for the dots.¹⁶⁾ On this premise, we assume that the dots either belong to a “large-size” group or a “small-size” group. The origin of the two peaks is therefore a consequence of thermal energy redistribution of carriers among the dots of the two groups. The qualitative descriptors of large- and small-size represent average dot dimensions. At low temperatures and moderate excitations, the source generates electron-hole pairs that predominantly tunnel to occupy the ground states of the “large-size” dots since these represent energy minima for the ensemble. This would explain why at 77 K, only a single emission peak is

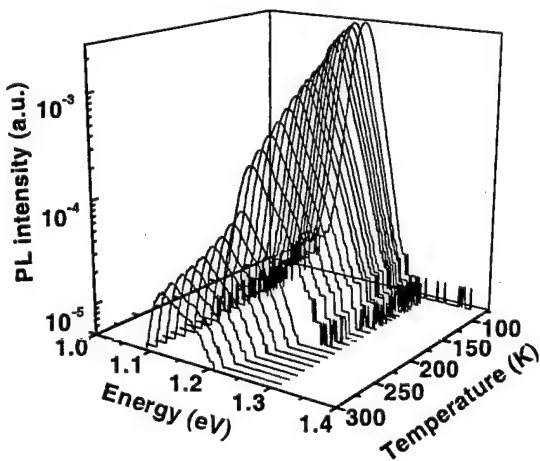


Fig. 1. Photoluminescence spectra of (In, Ga)As/GaAs quantum dots at different sample temperatures.

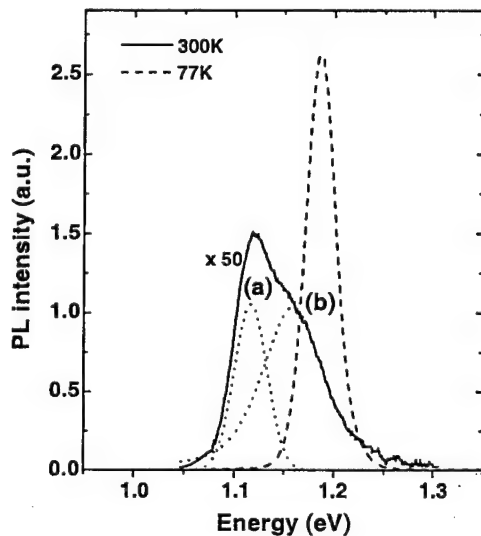


Fig. 2. Luminescence spectra of (In, Ga)As/GaAs quantum dots at 77 and 300 K.

observed at 1.19 eV. As the temperature is raised, however, thermal energy redistributes the carriers among the dots of different sizes, causing some to occupy the slightly higher ground states of the "small-size" dots. This becomes evident at room-temperature where the emission now is from both the "large-size" and "small-size" dots, leading to peaks at 1.12 and 1.16 eV. We interpret the higher energy emission to be from the "small-size" dots where the conduction (valence) band ground state energies, on the average, are positioned higher (lower) than those in the "large-size" dots.

The thermal redistribution of carriers in the dot ensembles can also be followed in another way. One can relate a relative shift of emission energies, $\Delta E_{\text{QD}}(T)$, from a fixed reference point to a variation in temperature. We consider a single low-temperature emission peak $h\nu(107 \text{ K})$ as the reference point. The relative shift is therefore defined as:

$$\Delta E_{\text{QD}}(T) = h\nu(T) - h\nu(107 \text{ K}), \quad (1)$$

where $h\nu(T)$ is the temperature-dependent peak. The relative shifts of the two spectra (a) and (b) of Fig. 2, as functions of temperature, are shown in Fig. 3. For comparison, we also show, as a solid line, the relative shift of the band gap energy of the $\text{In}_{0.23}\text{Ga}_{0.77}\text{As}$ material out of which the quantum dots are synthesized. This variation is calculated from

$$\Delta E_{\text{g}}(T) = E_{\text{g}}(T) - E_{\text{g}}(107 \text{ K}), \quad (2)$$

with the temperature variation of the band gap, $E_{\text{g}}(T)$, calculated according to Varshini's law.¹⁷⁾ In general, the peak luminescence energy of the quantum-dot ensemble should follow the thermal shrinkage of the band gap as the temperature is raised, as long as there is no transfer of carriers from one state to another. However, from Fig. 3, one observes that the relative rate of thermal shrinkage for spectra (a) and (b) is lower than that of the band gap, indicating a carrier transfer from low to high energy states. If

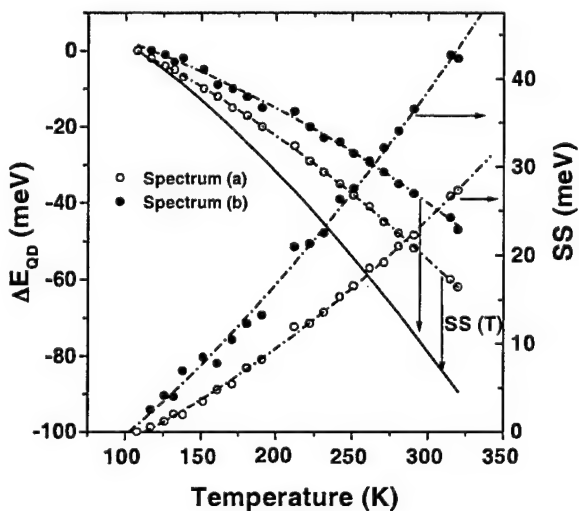


Fig. 3. Variation of the relative shift ΔE_{QD} (from the fixed reference point of the peak emission at 107 K) as a function of temperature for emission band (a) and (b) of Fig. 2. The solid line is the relative band gap variation of $(\text{In}, \text{Ga})\text{As}$, ΔE_{g} , with temperature. The Stokes shift (SS), defined as the variation of the difference between ΔE_{QD} and ΔE_{g} with temperature, is also shown on the right hand side of the figure.

the carrier transfer had been from high to low energy states, the relative thermal shrinkage rate would have been larger than that of the band gap.¹⁸⁾

The difference between ΔE_{QD} and ΔE_{g} can generally be considered to be the Stokes shift (SS) between the luminescence and absorption lines. This shift is shown in Fig. 3. Note that the Stokes shift for spectrum (b) of Fig. 2 is higher than that for spectrum (a), suggesting that the size distribution of dots corresponding to emission band (b) is larger than that for band (a). The inhomogeneous broadening of the luminescence spectrum depends on the size distribution; a large-size distribution gives rise to a broad spectral spread. This is evident in the luminescence spectra, where the spectral spread for band (b) is 61.7 meV—which is about twice the value (32.8 meV) for band (a).

To gain further insight into the thermal energy redistribution of carriers in the dot ensemble, we have plotted the ratio, R , of the integrated luminescence intensity for band (a) and (b) of Fig. 2 as a function of temperature. This ratio is shown in Fig. 4. The solid line through the points is an Arrhenius plot of the equation

$$R = A \exp\left(-\frac{\Delta E}{k_B T}\right). \quad (3)$$

The meaning of the symbols is discussed in the following. The activation energy $\Delta E \approx 38 \text{ meV}$. The data displayed in Fig. 4 can be explained if one assumes a quasi-equilibrium distribution of carriers between the "large" and "small" dots at high temperatures. The emission intensity from the large and small dots can be written, respectively, as:

$$I_{\text{large}} = B_{\text{large}} n_{\text{large}} p_{\text{large}}, \quad (4)$$

and

$$I_{\text{small}} = B_{\text{small}} n_{\text{small}} p_{\text{small}}, \quad (5)$$

where n and p are the electron and hole populations of the states in the dots, and B is a constant. If the carrier populations obey Boltzmann statistics at any temperature T , then the ratio R can be written as:

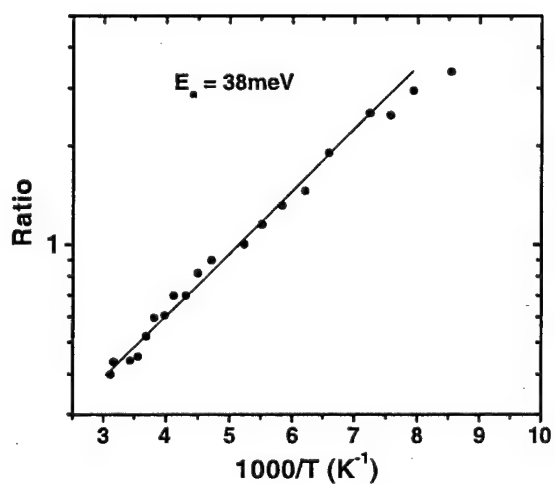


Fig. 4. The Arrhenius plot of the ratio of the integrated photoluminescence intensity of spectra (a) and (b); the solid line is a fit to the equation $R = A \exp(-\Delta E/k_B T)$.

$$R = \left(\frac{B_{\text{big}}}{B_{\text{small}}} \right) R_n R_p \exp \left(-\frac{\Delta E_n + \Delta E_p}{k_B T} \right) \approx A \exp \left(-\frac{\Delta E}{k_B T} \right), \quad (6)$$

where R_n and R_p are, respectively, the ratios of the electron and hole effective densities of states in the large- and small-size dots. The energy differences between electron and hole levels in the large- and small-size dots are, respectively, ΔE_n and ΔE_p . The energy difference between the emission bands from the large- and small-size dots is given by $\Delta E = \Delta E_n + \Delta E_p$. If the temperature dependence of B_{large} , B_{small} , R_n , and R_p is less than the exponential term, then the ratio R can be approximated as $\exp(-\Delta E/k_B T)$, which is consistent with the results displayed in Fig. 4. Note that the energy difference of 40 meV measured between the peaks of spectra (a) and (b) of Fig. 2 is quite close to the energy (38 meV) extracted as the activation from Fig. 4. These results suggest that the relative populations of carriers in the states of the dots of various sizes obey Boltzmann statistics. Similar results have been reported for undoped quantum dot samples.¹⁹

2.2 Intraband absorption

The energy spacing between sublevels within the conduction band of the quantum-dot ensemble can be probed by Fourier transform infrared spectroscopy. We have carried out such measurements for our samples and the low- and room-temperature absorption spectra are shown in Fig. 5. The spectra have been normalized by using the absorption of a (semi-insulating) GaAs substrate without quantum-dots polished in a manner similar to that of the quantum-dot samples. The low-temperature (77 K), normal-

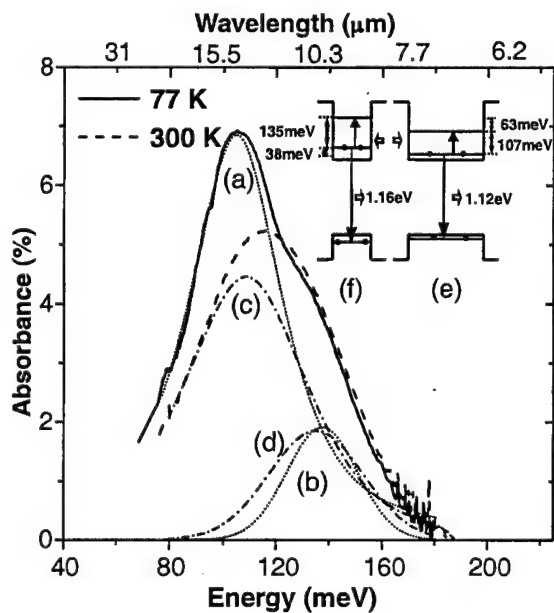


Fig. 5. Normal-incidence intraband absorption spectra of (In, Ga)As quantum dots at 77 and 300 K. The spectra (a), (b) and (c), (d) were obtained by deconvolution of the absorption spectra at 77 K and 300 K, respectively. The inset of this figure shows simplified band diagrams for large- and small-size dots. The energy levels derived from interband emission and intraband absorption measurements are also shown.

incidence absorbance for a five-period superlattice of $\text{In}_{0.23}\text{Ga}_{0.77}\text{As}/\text{GaAs}$ quantum dots was about 7%. The absorbance per quantum-dot superlattice period is therefore $\sim 1.4\%$. Weber *et al.*¹² have reported a low-temperature (77 K) absorbance per InAs/InAlAs quantum-dot period of 0.78%. In another report Phillips *et al.*,¹¹ measured a room-temperature (300 K) absorbance of about 0.48% per InAs/GaAs quantum-dot period. This absorbance is less than the value of 1.02% we obtain for our (In, Ga)As/GaAs quantum-dot structures at 300 K. We must emphasize that it is difficult to compare absorbances of samples with different constituents in the superlattice periods.

The spectra displayed in Fig. 5 suggest that the room- and low-temperature absorption spectra can be resolved into two resonances. At liquid nitrogen temperature (77 K), the absorption has resonances at 105 meV [curve (a)] and 137 meV [curve (b)]. At 300 K, the absorption curve can be resolved to reveal resonances at 107 and 135 meV. The integrated absorbance for the peak which moves from 105 to 107 meV decreases while that for the peak that goes from 135 to 137 meV increases as the temperature is increased from 77 to 300 K. This is likely to be due to the escape of carriers from the ground states of the large-size dots to the higher lying ground states of the small-size dots. The integrated absorbance of the large-size dots (at 105 and 107 meV), therefore decreases as carriers escape from these dots into the small-size dots. On the other hand, the integrated absorbance of the small-size dots (at 135 and 137 meV) increases. On the basis of our photoluminescence emission and intraband absorption data, a simplified energy structure for the large and small dots can be derived; such an energy scheme is shown in the inset of Fig. 5. Here, we have assumed that the energy difference between the ground states in the valence band of the large and small size dots is about 2 meV. From an analysis of the photoluminescence emission intensity as a function of temperature, it was shown that in the conduction band, the ground state of the small-size dots lies about 38 meV above the ground state of the large-size dots.

The spectral spreads of the absorption spectra in Figs. 5(a), 5(b), 5(c), and 5(d) are, respectively, 42.5, 31.3, 54.8, and 41.8 meV. These linewidths, like those for the interband transitions, are a result of homogeneous and inhomogeneous broadening processes in the dot ensembles. Homogeneous broadening generally gives rise to a Lorentzian line-shape. Inhomogeneous broadening, which is mostly due to size distribution effects in dot population, gives rise to a Gaussian line-shape. The emission and absorption spectra obtained for our quantum-dot structures could not be fitted very well to either a pure analytic Lorentzian line-shape or a pure Gaussian line-shape. The experimental spectra could only be fitted to a mixture of both a Lorentzian and a Gaussian. This fact is further evidence of the presence of size distribution in the dot ensemble.

3. The Electronic Energy Structure of the Dots

The energy structure of the dots depends on the strain distribution around and inside the dots. Among the factors that affect this are the shape and size of the dots. The dots synthesized in our laboratory have truncated pyramidal shapes. They typically lie on top of a wetting layer whose

thickness in the structures studied here is about 5 nm. The average lateral extent of the dots is about 16–20 nm; the height is about 3 nm.

The first step in any theoretical analysis of the electronic structure of the dots is the determination of the strain distribution. The details of the analytical approach for determining the strain field of pyramidal quantum dots with truncated tops have been presented elsewhere²⁰⁾ and only the salient points will be given here. We use an analytical approach based on the continuum elasticity method pioneered by Eshelby²¹⁾ for calculating the strain distribution due to a uniformly lattice-mismatched inclusion. First, a set of vectors \mathbf{A} as identified by Downes *et al.*²²⁾ is defined; this set of vectors is defined such that $\nabla \cdot \mathbf{A}$ yields the Green's function for the stress components, σ^{sph} , corresponding to a spherical point inclusion. Thus

$$\sigma_{ij}^{\text{sph}} = \nabla \cdot \mathbf{A}_{ij}. \quad (7)$$

The potential components can then be written, according to Grundmann *et al.*¹⁴⁾ as:

$$\begin{aligned} \mathbf{A}_{ij}(x, y, z) &= -\frac{1}{4\pi} \frac{E\varepsilon_0}{1-\nu} \frac{x_i e_i}{(x^2 + y^2 + z^2)^{3/2}} \\ \mathbf{A}_{ij}(x, y, z) &= -\frac{1}{2} \frac{1}{4\pi} \frac{E\varepsilon_0}{1-\nu} \frac{x_i e_j + x_j e_i}{(x^2 + y^2 + z^2)^{3/2}} \end{aligned} \quad (8)$$

where (i, j) are replaced by (x, y, z) , and e_i is the unit vector in the i -th direction. Because of the linear superposition of stresses,

$$\begin{aligned} \sigma_{ij}^V(x, y, z) &= \iiint_V \sigma_{ij}^{\text{sph}}(x - x_0, y - y_0, z - z_0) dV(x_0, y_0, z_0) \\ &= \iiint_V \nabla \cdot \mathbf{A}(x - x_0, y - y_0, z - z_0) dV(x_0, y_0, z_0). \end{aligned} \quad (9)$$

Applying the divergence theorem, with (x_0, y_0, z_0) a point within the volume of the dot, the stress field due to an arbitrarily shaped, uniformly lattice-mismatched quantum dot contained within an isotropic, elastic medium is obtained by calculating the following integral, where (x_0, y_0, z_0) is now a point on the surface of the quantum dot. Thus

$$\begin{aligned} \sigma_{ij}^V(x, y, z) &= \iint_S \mathbf{A}_{ij}(x - x_0, y - y_0, z - z_0) dS(x_0, y_0, z_0) \\ &+ \delta_{ij} \frac{E\varepsilon_0}{1-\nu} \iint_V \delta(x - x_0, y - y_0, z - z_0) \\ &\times dV(x_0, y_0, z_0), \end{aligned} \quad (10)$$

where ε_0 is the lattice-mismatch, E is Young's modulus, ν is Poisson's ratio, V is the volume of the quantum dot, and δ_{ij} is the Kronecker delta. The last part of eq. (10) comes from evaluating the limit of the surface integral, as the field point (x, y, z) approaches the boundary at position (x_0, y_0, z_0) . The misfit strain (lattice-mismatch) is taken as negative for a material under compression, such as InAs on top of GaAs or $\text{In}_x\text{Ga}_{1-x}\text{As}$ on GaAs. The volume of a square-based, truncated pyramid is defined by

$$\begin{aligned} -b \frac{(H-z)}{2H} &\leq x \leq b \frac{(H-z)}{2H} \\ -b \frac{(H-z)}{2H} &\leq y \leq b \frac{(H-z)}{2H}, \\ 0 &\leq z \leq Ht \end{aligned} \quad (11)$$

where H is the height of the pyramid in the absence of truncation, b is the base of the pyramid, t represents the degree of truncation (approximately 0.64 in the present case), and $h = Ht$ is the height of the truncated pyramid. The origin of coordinates is at the center of the base and the z -axis is the growth direction. The strains follow from substitution of stresses into Hooke's law:

$$\varepsilon_{ij} = \frac{1}{E} [(1+\nu)\sigma_{ij} - \delta_{ij}\nu\sigma_{kk}]. \quad (12)$$

We can define the hydrostatic and biaxial strains as

$$\varepsilon_h = \varepsilon_{xx} + \varepsilon_{yy} + \varepsilon_{zz}, \quad (13)$$

and

$$\varepsilon_b = \varepsilon_{zz} - \frac{1}{2}(\varepsilon_{xx} + \varepsilon_{yy}). \quad (14)$$

The calculated strain tensor for quantum dots with a base width of 16.8 and 19.7 nm, respectively are shown in Figs. 6 and 7, in the x - z plane. The effect of the strain profile on the electronic structure of the quantum dots can be qualitatively understood by examining the strain-modified band offsets. The strain-induced shift in the conduction band depends on the hydrostatic component of the strain through

$$\delta E_c = a_c(\varepsilon_{xx} + \varepsilon_{yy} + \varepsilon_{zz}), \quad (15)$$

where a_c is the deformation potential for the conduction band. The offset of the unstrained conduction band as a function of indium mole fraction, x , is given by,²³⁾

$$E_c^0(x) = E_{v,av}^0(x) + \frac{\Delta_0(x)}{3} + E_g(x) \quad (16)$$

where $\Delta_0(x)$ is the spin-orbit splitting, and $E_g(x)$ is the unstrained energy band gap. The conduction and valence band-edges are determined, respectively, from the following relations:

$$E_c(x) = E_c^0(x) + \delta E_c(x), \quad (17)$$

$$E_v^{\text{hh}}(x) = E_{v,av}^0(x) + \frac{\Delta_0(x)}{3} + \delta E_{v,h}(x) - \frac{1}{2} \delta E_{v,b}(x), \quad (18)$$

and

$$\begin{aligned} E_v^{\text{lh}}(x) &= E_{v,av}^0(x) - \frac{\Delta_0(x)}{3} + \delta E_{v,h}(x) - \frac{1}{4} \delta E_{v,b}(x) \\ &+ \frac{1}{2} \sqrt{\Delta_0^2(x) + \Delta_0(x)\delta E_{v,b}(x) + \frac{3}{4} [\delta E_{v,b}(x)]^2}. \end{aligned} \quad (19)$$

In the equations above,

$$\delta E_{v,h}(x) = a_v(\varepsilon_{xx} + \varepsilon_{yy} + \varepsilon_{zz}), \quad (20)$$

and

$$\delta E_{v,b}(x) = 2b(\varepsilon_{zz} - \varepsilon_{xx} - \varepsilon_{yy}). \quad (21)$$

$E_{v,av}^0(x)$ is the unstrained average valence band, a_v and b are the valence band deformation potentials,²⁴⁾ as described in Table I.

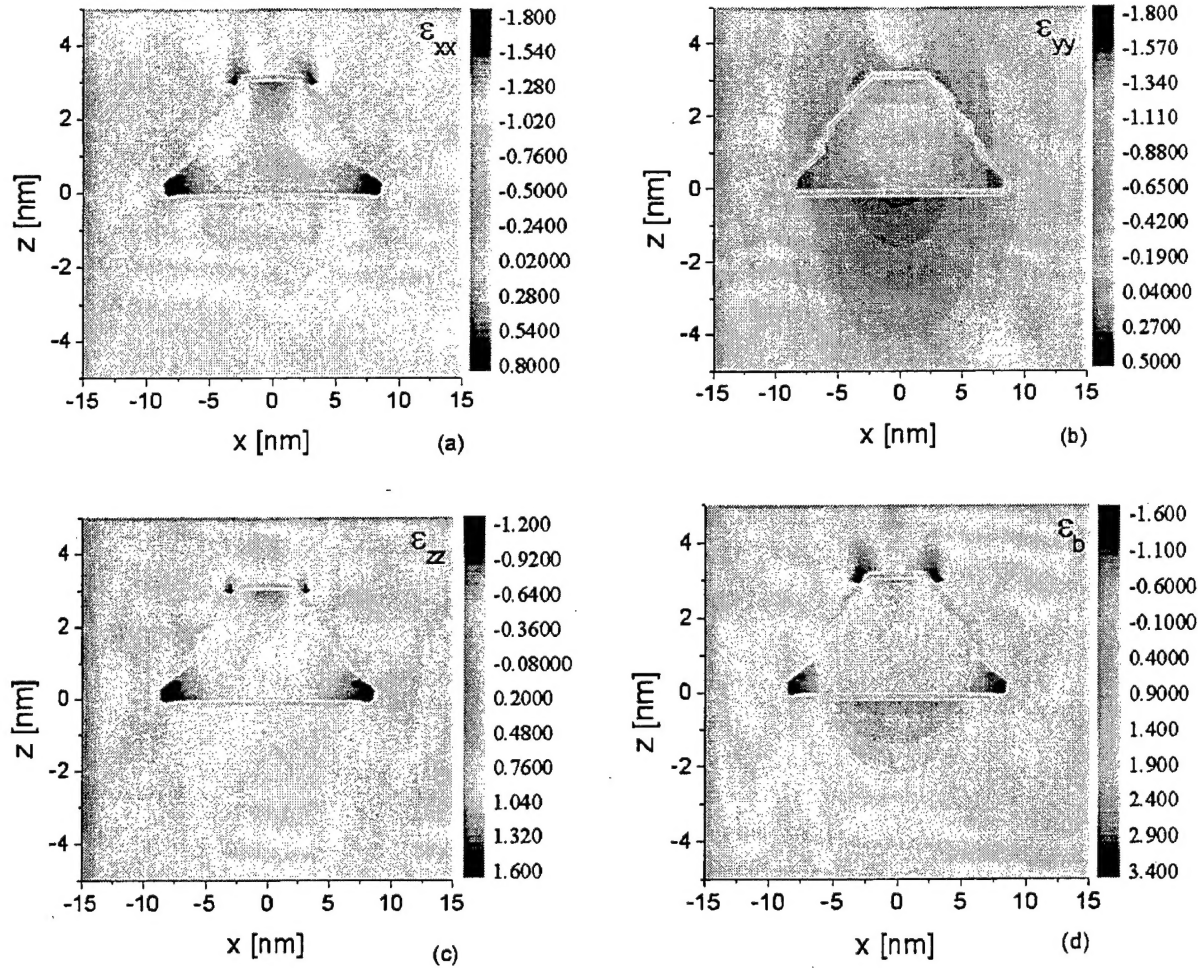


Fig. 6. The strain field map calculated for the x - z plane for dots with a base width of 16.8 nm: (a) ϵ_{xx} , (b) ϵ_{yy} , (c) ϵ_{zz} , and (d) $\epsilon_b = \epsilon_{zz} - (\epsilon_{xx} + \epsilon_{yy})/2$.

The carriers confining potentials can now be determined from

$$V^e = E_c(x) - E_c(x=0),$$

$$V^{hh} = E_v^{hh}(x=0) - E_v^{hh}(x),$$

and

$$V^h = E_v^h(x=0) - E_v^h(x), \quad (22)$$

where $x=0$ describes the conditions inside the GaAs matrix (with no indium), and $x \neq 0$ reflects the properties inside the $\text{In}_x\text{Ga}_{1-x}\text{As}$ quantum dot.

The material parameters used in our calculations are summarized in Table I. Several different models have been developed to calculate the electronic structure of $\text{In}_x\text{Ga}_{1-x}\text{As}$ dots.^{14,25-27} Here, we use an eight-band $k\cdot p$ description, with strain effects included via deformation potential theory.²⁴ The eight-band Luttinger-Kohn parameters are calculated according to the approach used by Pollak²⁸ and Bir *et al.*²⁹ The bound states of the quantum dots are found by numerically solving the Schrödinger equation, which, in the effective-mass approximation, is written as

$$-\frac{\hbar^2}{2} \nabla \left(\frac{1}{m_i^*(r)} \right) \nabla \Psi_n(r) + V(r) \Psi_n(r) = E \Psi_n(r). \quad (23)$$

In the expression above, $m_i^*(r)$ is replaced by $m_{\text{InGaAs}}^*(r)$ inside the dot, and by $m_{\text{GaAs}}^*(r)$ in the GaAs matrix material. The parameter $V(r)$ is the three-dimensional confining potential. In the frame of the eight-band model, the wave function can be expanded as

$$\Psi_n(r) = \sum_{j=1}^8 F_{nj}(r) u_j(r). \quad (24)$$

As described by Stier *et al.*,²⁴ the $k\cdot p$ model has a few drawbacks when it is applied to nanostructures. These drawbacks are related to the fixed number of Bloch functions used in synthesizing the wavefunction (eight in the eight-band formalism). The problems are also connected with the restriction to the Brillouin zone center, Γ , and the assumption of the same Bloch functions, regardless of material and strain variations. The choice of the appropriate boundary conditions and the arbitrariness of the matching conditions for the envelope functions across the heterointerface are also issues to be concerned with. In our case, we use the guidelines developed by Burt³⁰ for the exact envelope-

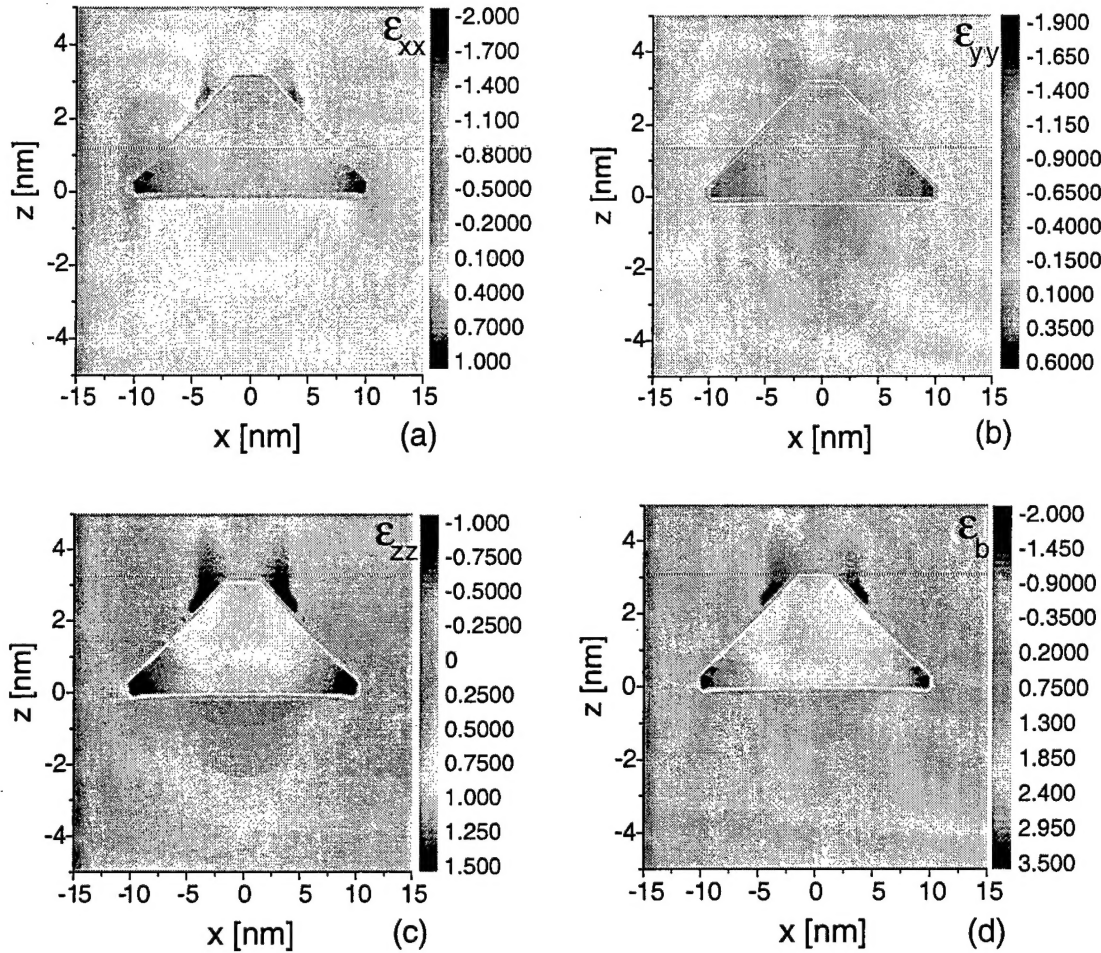


Fig. 7. The strain field map calculated in the x - z plane for dots with a base width of 19.7 nm: (a) ε_{xx} , (b) ε_{yy} , (c) ε_{zz} , and (d) $\varepsilon_b = \varepsilon_{zz} - (\varepsilon_{xx} + \varepsilon_{yy})/2$.

Table I. Material parameters used in theoretical calculations.

Parameter	GaAs	InAs	$In_xGa_{1-x}As$
a (Å)	5.6503	6.0553	$5.6503 + 0.405x$
E_g (eV)			
6.4 K	1.518	0.413	$1.518 - 1.580x + 0.475x^2$
300 K	1.424	0.324	$0.324 + 0.7(1-x) + 0.4(1-x)^2$
Δ_0 (eV)	0.340	0.380	$0.340 - 0.093x + 0.133x^2$
C_{11} (N/m ²)	11.88	8.33	$11.88 - 3.55x$
C_{12} (N/m ²)	5.38	4.53	$5.38 - 0.85x$
a_c (eV)	-8.013	-5.08	$-8.013 + 2.933x$
a_v (eV)	1.16	1.00	
b (eV)	-1.7	-1.8	
$E_{v,av}^0$ (eV)	-6.92	-6.747	$-6.92 + 0.231x - 0.058x^2$
m_e^*	$0.0667 m_0$	$0.02226 m_0$	$0.0667 - 0.0419x - 0.00254x^2$

function theory by taking into account the variation of mass parameters from their bulk values due to strain-induced band deformations.

Equation (23) can be solved for the eigenvalues and eigenfunctions of the system by invoking periodic boundary

Small dots (b=16.8 nm) Big dots (b=19.7 nm)

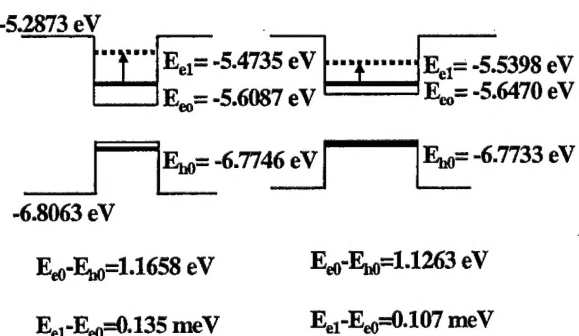


Fig. 8. Schematic representation of calculated energy levels (referenced to the vacuum level) for quantum dots with base widths of 16.8 nm and 19.7 nm, respectively. The fundamental interband transition energies, $(E_{e0} - E_{h0})$, and the intraband transition energies, $(E_{el} - E_{e0})$, are also shown.

conditions, expanding $\Psi_n(r)$ in terms of normalized plane-wave states, and diagonalizing the resulting matrix. This

approach has also been used by Cusack *et al.*,²⁵ it does not require the matching of the wavefunctions across the boundary between the dot and the matrix material. This makes the method useful when arbitrary (position dependent) confining potentials are involved. The boundary conditions would only require that the states do not overlap significantly for neighboring dots.

The energy levels of the truncated pyramidal-shaped $\text{In}_{0.23}\text{Ga}_{0.77}\text{As}$ quantum dots have been calculated using the parameters listed in Table I. The conduction ground state energy level for dots with a base of $b = 19.7 \text{ nm}$ is calculated to be $E_{c0} = -5.647 \text{ eV}$ (measured from the vacuum level); the first excited state for electrons is located at $E_{e1} = -5.540 \text{ eV}$. For the heavy holes, the ground state energy (measured from the vacuum level) is located at $E_{h0} = -6.773 \text{ eV}$. The fundamental transition energy, $(E_{e0} - E_{h0})$, is therefore 1.126 eV . The separation between the conduction band ground state and the first excited state has been calculated as 107 meV .

For small dots, characterized by a base dimension $b = 16.8 \text{ nm}$, the ground state for electrons is calculated as $E_{e0} = -5.474 \text{ eV}$ (as measured from the vacuum level); the first excited state is located at $E_{e1} = -5.609 \text{ eV}$. For the heavy-holes, the ground state energy (measured from the vacuum level) is $E_{h0} = -6.775 \text{ eV}$. The fundamental transition energy, $(E_{e0} - E_{h0})$, is therefore 1.166 eV . The separation between the conduction ground state and the first excited state is evaluated as 135 meV . The conduction ground state of the small-size dots is calculated to lie about 38.4 meV above the ground state of large-size dots. All the calculated energy levels are shown in Table II; they are also displayed in Fig. 6 in a simple energy band diagram. The results of the calculations performed here are in good agreement with the photoluminescence, as well as infrared absorption data obtained at 300 K .

We want to emphasize that the dot-sizes chosen for the calculations are not unique. The strain-modified confined energy levels are not as sensitive to variation of the height of the dot as they are to the change of the base length of the structure. Although other combinations of the base and height might yield similar ground state energy levels, a unique spectrum (ground state and excited states for both electrons and heavy holes) would be obtained only for a particular combination of these dimensions. Our choice of dimensions in this work was guided by measurements obtained from transmission electron microscope images of the dots. The final choice was guided by the experimental transition energies obtained from the photoluminescence and absorption measurements we performed.

Table II. Theoretically calculated energy levels, along with the experimentally determined interband emission and intraband absorption energies.

	Base width = 19.7 nm		Base width = 16.8 nm	
	Interband emission	Intraband absorption	Interband emission	Intraband absorption
Experimental	1.12 eV	107 meV	1.16 eV	135 meV
Theoretical	1.126 eV	107 meV	1.166 eV	135 meV

4. Summary

In summary, we have presented results of our optical study of the thermal redistribution of carriers in quantum-dot ensembles of various sizes. Using an analytical approach, we have calculated the energy levels in the dots and found that the theoretical results are in agreement with our experimental data.

Acknowledgments

This work is supported by the US Army Research Office, Research Triangle Park, North Carolina and by the US Army Research Laboratory, Adelphi, Maryland.

- 1) F. Heinrichsdorff, Ch. Ribbat, M. Grundmann and D. Bimberg: *Appl. Phys. Lett.* **76** (2000) 556.
- 2) K. Imamura, Y. Sugiyama, Y. Nakata, S. Muto and N. Yokoyama: *Jpn. J. Appl. Phys.* **34** (1995) L1445.
- 3) D. Pan, E. Towe and S. Kennerly: *Appl. Phys. Lett.* **73** (1998) 1937.
- 4) R. L. Sellin, Ch. Ribbat, M. Grundmann, N. N. Ledentsov and D. Bimberg: *Appl. Phys. Lett.* **78** (2001) 1207.
- 5) S. Maimon, E. Finkman, G. Bahir, S. E. Schacham, J. M. Garcia and P. M. Petroff: *Appl. Phys. Lett.* **73** (1998) 2003.
- 6) D. Pan, E. Towe and S. Kennerly: *Appl. Phys. Lett.* **76** (2000) 3301.
- 7) D. I. Lubyshev, P. P. Gonzalez-Borrero, E. Marega, Jr., E. Petiprez, N. la Scala, Jr. and P. Basmajian: *Appl. Phys. Lett.* **68** (1996) 205.
- 8) R. P. Mirin, J. P. Ibbetson, K. Nishi, A. C. Gosard and J. E. Bowers: *Appl. Phys. Lett.* **67** (1995) 3795.
- 9) S. Fafard, S. Raymond, G. Wang, R. Leon, D. Leonard, S. Charbonneau, J. L. Merz, P. M. Petroff and J. E. Bowers: *Surf. Sci.* **361** (1996) 778.
- 10) L. Chu, A. Zrenner, G. Böhm and G. Abstreiter: *Appl. Phys. Lett.* **75** (1999) 3599.
- 11) J. Phillips, P. Bhattacharya, S. W. Kennerly, D. W. Beckman and M. Datta: *IEEE J. Quantum Electron.* **35** (1999) 936.
- 12) A. Weber, O. Gauthier-Lafaye, F. H. Julien, J. Brault, M. Gendry, Y. Désieres and T. Benyatton: *Appl. Phys. Lett.* **74** (1999) 413.
- 13) P. Hawrylak, A. Wojs, D. J. Lockwood and P. D. Wang: *Surf. Sci.* **361** (1996) 774.
- 14) M. Grundmann, O. Stier and D. Bimberg: *Phys. Rev. B* **52** (1995) 11969.
- 15) L. R. C. Fonseca, J. L. Jimenez and J. P. Leburton: *Phys. Rev. B* **58** (1998) 9955.
- 16) H. Xu, Q. Gong, B. Xu, W. Jiang, J. Wang, W. Zhou and Z. Wang: *J. Cryst. Growth* **200** (1999) 70.
- 17) Y. P. Varshni: *Physica* **34** (1967) 149.
- 18) A. Polimeni, A. Patanè, M. Henini, L. Eaves and P. C. Main: *Phys. Rev. B* **59** (1999) 5064.
- 19) A. Patanè, A. Polimeni, P. C. Main, M. Henini and L. Eaves: *Appl. Phys. Lett.* **75** (1999) 814.
- 20) V. G. Stoleru, D. Pal and E. Towe: submitted to *Physica E* (2001).
- 21) J. Eshelby: *Proc. R. Soc. London, Ser. A* **241** (1957) 376.
- 22) J. R. Downes, D. A. Faux and E. P. O'Reilly: *J. Appl. Phys.* **81** (1997) 6700.
- 23) G. Cipriani, M. Rosa-Clot and S. Taddei: *Phys. Rev. B* **61** (2000) 7536.
- 24) O. Stier, M. Grundmann and D. Bimberg: *Phys. Rev. B* **59** (1999) 5688.
- 25) M. Cusack, P. R. Briddon and M. Jaros: *Phys. Rev. B* **54** (1996) R2300.
- 26) J. Kim, L.-W. Wang and A. Zunger: *Phys. Rev. B* **57** (1998) R9408.
- 27) J.-Y. Marzin and G. Bastard: *Solid State Commun.* **92** (1994) 437.
- 28) F. H. Pollak: *Semicond. Semimet.* **32** (1990) 17.
- 29) G. L. Bir and G. E. Pikus: *Symmetry and Strain-Induced Effects in Semiconductors* (Wiley, New York, 1974).
- 30) M. G. Burt: *J. Phys.: Condens. Matter* **4** (1992) 6651.